THESIS FOR THE DEGREE OF LICENTIATE OF ENGINEERING

Metallic materials in Solid Oxide Fuel Cells: Oxidation and chromium evaporation properties

MAREDDY JAYANTH REDDY

Department of Chemistry and Chemical Engineering
Division of Energy and Materials
CHALMERS UNIVERSITY OF TECHNOLOGY
Gothenburg, Sweden 2021

Metallic materials in Solid Oxide Fuel Cells: Oxidation and chromium evaporation properties
MAREDDY JAYANTH REDDY

© MAREDDY JAYANTH REDDY, 2021

Thesis for the degree of Licentiate of Engineering 2021:14
Department of Chemistry and Chemical Engineering
Division of Energy and Materials
Chalmers University of Technology
SE-412 96 Gothenburg
Sweden
Telephone: +46 (0)31-772 1000

Cover:
SEM cross-section micrograph and EDX maps of Ce/Co coated 441 exposed at 800 °C for 1000 h.

Chalmers Reproservice
Gothenburg, Sweden 2021

Abstract

Solid oxide fuel cells (SOFCs) are high-temperature energy conversion devices which have great potential due to their high efficiency, low operating costs and flexibility in using conventional hydrocarbon based fuels. However, system cost, durability and performance stability in long-term operation are barriers to the widespread commercialization of SOFC technology.

Due to the high-temperature operation and aggressive environment in SOFCs, metallic materials - used for interconnects and balance of plant (BOP) - are subject to corrosion. Interconnects are typically made of ferritic stainless steel, which forms a protective chromia scale at high temperatures. This results in two main degradation mechanisms: 1) chromium evaporation, which leads to cathode poisoning and 2) chromia scale growth, which leads to increased electrical resistance. To date, research into metallic materials in SOFC has focused mostly on interconnects. However, metallic materials used in BOP components can be a significant source of volatile chromium species and are often overlooked. The aim of this thesis is to find high performance, cost-effective metallic materials for SOFC systems. Five metallic materials AISI 441, AISI 444, A197/Kanthal® EF101, alloy 800H and alloy 600, were studied for potential use in BOP components. Low-cost steels, AISI 441 and AISI 444, and tailor-made Crofer 22 APU in combination with different coatings were evaluated for the interconnect application. Chromium evaporation and oxide-scale growth of the materials are investigated, and the oxide scale is studied further, using XRD, SEM, EDX and ASR.

The alumina former, A197, showed the lowest chromium evaporation and oxidation in all exposure conditions. Alloy 800H showed poor oxidation behaviour at lower temperatures but its performance improved significantly after pre-oxidation. Alloy 800H has higher chromium evaporation than A197 but significantly lower than 441 and 444. This low chromium evaporation is due to the formation of an Fe, Ni-rich oxide cap layer. Alloy 600 showed intermediate performance. 441 and 444 showed the highest oxidation and chromium evaporation of the selected alloys, making them a poor choice for BOP components.

The uncoated low-cost steels, 441 and 444, showed higher chromium evaporation and/or oxide scale growth than the tailor-made Crofer 22 APU. The oxide scale structure was similar for all the steels, with $(Cr, Mn)_3O_4$ spinel on top and Cr_2O_3 scale underneath after 500 hours. The Ce/Co coated steels showed lower oxide scale growth and a chromium evaporation at least 60 times lower than the uncoated steels. In addition, all the coated steels showed similar chromium evaporation, oxide scale structure ($(Co, Mn)_3O_4$ spinel on top and Cr_2O_3 scale underneath), oxide scale thickness and area specific resistance after 1,000 hours.

Keywords: SOFC, Interconnect, Balance of Plant, High temperature corrosion, Chromium evaporation

List of publications

This thesis is based on the work contained in the following publications:

Publication 1 Reddy, M. J., Svensson, J. E. and Froitzheim, J. "Evaluating candidate materials for balance of plant components in SOFC: Oxidation and Cr evaporation properties" in *Corrosion Science* **190** (2021) https://doi.org/10.1016/j.corsci.2021.109671

Publication 2 Reddy, M. J., Svensson, J. E. and Froitzheim, J. "Reevaluating the Cr Evaporation Characteristics of Ce/Co Coatings for Interconnect Applications" *ECS Transactions.* **103**, 1899–1905 (2021)

Publication 3 Reddy, M. J., Svensson, J. E. and Froitzheim, J. "Evaluation of Ce/Co coated FeCr steels for SOFC interconnects", *Manuscript.*

Statement of author's contribution

I was the main author of all the appended publications. For the publication 1, I did most of the experimental work and microstructural analysis using the scanning electron microscope. Florian Le Briquer did exposures on alloy 800H and A197 under my supervision. For publications 2 and 3, I did all the experimental work and analytical charecterization.

Acknowledgements

Throughout the work leading to this licentiate thesis, I have received much support and help. I would like to take this opportunity to acknowledge everyone.

First and foremost, I would like to thank my supervisors, Prof. Jan Froitzheim and Prof. Jan-Erik Svensson, for allowing me to carry out the work of this thesis at Chalmers University of Technology. Your expertise was invaluable in formulating the research topic and approach. Your guidance and feedback along the way were constructive and extremely helpful. In addition, I would like to thank my examiner, Prof. Lars-Gunnar Johansson and my directors of studies, Prof. Lars Evenäs and Prof. Itai Panas, for their support and discussions during my research.

Furthermore, I would like to thank my colleagues (current and former) in the Fuel Cell Group (FCG); Alberto Visibile, Matthieu Tomas, Claudia Göbel, Luca Gagliani, Camilla Cossu, Kereem Ozgur Gunduz, Anton Chyrkin and Hannes Falk-Windisch. Thank you for creating a safe, friendly work environment and for initiating many intriguing discussions and collaborations. My heartfelt gratitude goes to Esraa Hamdy, Christine Geers and Tommy Sand for their valuable input and for helping me with my experiments. A Special thanks go to my interns, Florian Le Briquer and Thibaut Chausson, for taking part in my work and assisting in producing relevant results.

I would like to thank everyone at the High Temperature Corrosion Centre (HTC) and the Department of Environmental Inorganic chemistry for their help, support, and for making me feel welcomed. I would also like to thank the HTC and the European project LowcostIC for their financial support. I would also like to acknowledge our industrial partners for providing us with interesting research questions and good discussions.

Last but not least, I would like to acknowledge my family and friends. A big thank you to my parents, sister and my wife for supporting me in my decision to pursue a PhD. Without their constant support and motivation, this would have never been possible.

Contents

1 Introduction

1.1 Motivation

Our primary energy sources for generating electricity and heat are fossil fuels such as coal, oil and natural gas. Fossil fuel consumption leads to greenhouse gas emissions. These are considered the leading cause of global warming, resulting in climate change. Economic growth and rising population are increasing global energy demand and accelerating climate change. Only one-third of primary energy is converted into usable energy (such as electricity and heat), and the rest is lost in the conversion process. For these reasons, alternative energy sources and energy conversion devices are essential to meet increasing demand and reduce emissions.

Fuel cells are considered a promising technology for future electricity needs. Fuel cells electrochemically convert the chemical energy of a fuel directly into electricity at a much higher efficiency than a combustion engine. They also have excellent part-load performance characteristics, lower emissions, and silent operation, making them attractive for distributed power generation. The most widely-used fuel cell type is the proton exchange membrane fuel cell (PEMFC). It uses hydrogen as fuel and requires expensive catalysts such as platinum to operate. However, it is extremely sensitive to impurities in the fuel which limits its applicability. By contrast, fuel cells such as solid oxide fuel cells (SOFC) operate on the same principle but at a higher temperature. This results in higher fuel flexibility. SOFCs can operate on hydrocarbons and may thus use existing infrastructure, making for a smoother transition from fossil based fuels to renewable fuels. System efficiencies as high as 90% may be achieved using SOFC based combined heat and power (CHP) systems [1]. High costs and degradation are major hurdles for the widespread commercialization of SOFC technology. The present work addresses the challenges of using metallic materials in SOFCs.

In SOFCs, metallic materials are mainly used in the interconnects and balance of plant (BOP) components. Interconnects are used to electrically connect the individual cells to form a fuel cell stack. Ceramic interconnects are replaced with metallic ones, to reduce costs and improve performance. Ferritic stainless steels (FSS) are used because they represent a compromise between cost and the required material properties. Nevertheless, the contribution of the interconnect to the overall stack cost is significant [2, 3]. At the high operating temperatures of SOFCs (600-900 °C), FSS undergo high-temperature oxidation, increasing the electrical resistance across the cell. Moreover, the chromia scale reacts with the atmosphere to form volatile Cr species which poison the cathode and degrade cell performance. To overcome these issues, tailor-made alloys are developed for interconnect applications. However, these are expensive and increase the overall cost of the system. One way to mitigate corrosion on the FSS is to apply protective coatings. From an economic point of view, combining low-cost steel with a coating is promising approach. Therefore, it is important to investigate the performance of low-cost steels and compare them with tailor-made alloys.

In addition to interconnects, metallic materials are also used in other parts of the SOFC system that are exposed to high temperatures. Balance of plant (BOP) - consisting of cathode preheater, heat recuperator, tubing, fuel processor, assembly components and so on - are auxiliary components supporting the functioning of a SOFC system. Metallic materials used outside the fuel cell stack can be a source of volatile chromium species. Owing to complex geometries, using coatings to prevent chromium evaporation on interconnects is challenging to implement in BOP components. Since the BOP components can make up to 75% of the total system cost [3], it is vital to find suitable, cost-effective materials for use in the BOP.

1.2 Aim

Material costs and service life are critical factors preventing the widespread commercialization of SOFC systems. Driving down costs requires cheaper materials with improved performance and reliability. The present thesis aims to find suitable low-cost materials for BOP components and coating-steel combinations for interconnects.

In the study focusing on BOP components, alloys from different material groups are selected and investigated in the air atmosphere. The evaluation focuses on the chromium evaporation and oxidation properties of these materials at different temperatures and surface conditions.

In the study focusing on interconnect materials, various steels and coating-steel combinations are investigated, to understand oxidation behaviour, chromium evaporation and electrical behaviour. Low-cost steels such as 441 and 444 are compared with tailor-made Crofer 22 APU.

2 Background

2.1 Fuel Cells

2.1.1 Introduction to fuel cells

Fuel cells convert the chemical energy in the fuel directly into electrical energy with very high efficiency. The history of fuel cells spans over two centuries. After water electrolysis was first described by British scientists Sir Anthony Carlisle and William Nicholson in 1800, reverse electrolysis was discovered by Sir William Grove and Christian Friedrich Schönbein in 1839 [4]. The scientists used the 'gas battery' to prove that an electrochemical reaction between hydrogen and oxygen could produce an electric current. Another essential contribution to fuel cells came in the early 20^{th} century from Wilhelm Ostwald, who provided much of the theoretical understanding on the fuel cell operation [5].

The basic principle behind the working process in a fuel cell is to decompose a chemical reaction while limiting the electrical transfer by inhibiting the free exchange of electrons. Electron transfer from fuel species to oxidant species is forced through an external circuit, called electric current. The functioning of fuel cells is similar to that of a battery, where a chemical redox reaction is locally separated into an oxidation reaction and a reduction reaction. However, the main difference is that the battery stores and releases energy; the fuel cell, on the other hand, generates energy from the fuel.

The basic overall reaction for fuel cells is the hydrogen combustion reaction shown in Equation 2.1.

$$H_2 + \frac{1}{2}\, O_2 \rightarrow\ H_2O + energy; \quad \Delta G^o = 237.09\ kJmol^{-1}[5] \tag{2.1}$$

The hydrogen combustion reaction is divided into two electrochemical half-reactions, oxidation and reduction. The electrolyte separates the fuel and air, and the electrochemical half-reactions, oxidation and reduction, occur at the electrodes, anode and cathode, respectively. The electrolyte mediates the electrochemical reaction by conducting specific ion/ions at a high rate while limiting the transfer of electrons. This forces the electrons to flow through an external circuit connecting the electrodes to complete the reaction. The flow of the electrons through the external circuit is harnessed as the electric current.

Compared to the fuel cell, in a combustion engine, the chemical energy in the fuel is first converted to heat, then to mechanical energy, and finally to electricity. The series of intermediate steps is complex and inefficient, which reduces the overall efficiency. The direct conversion of chemical energy to electrical energy in a fuel cell eliminates the inefficient intermediate stages of the conventional combustion process. Therefore, the efficiency of a fuel cell is not limited by the Carnot cycle, as is the case with a conventional

combustion process. The efficiency of a conventional combustion power plant is about 30% [6], while fuel cells can achieve an electrical efficiency of up to 65% [4]. Due to the absence of mechanical processes in a fuel cell, the operation is silent, reducing noise pollution. In addition, wear and tear are low, resulting in lower maintenance requirements and higher reliability of the system. The emissions such as particulates, NO_x and SO_x are extremely low due to the lack of combustion. Despite these intriguing advantages, the implementation of fuel cell technology is rather limited to very few applications. Fuel cells are quite expensive due to the low production volumes. Due to the complex electrochemical processes and interfaces, fuel cells are susceptible to environmental poisons.

2.1.2 Types of Fuel cells

There are several types of fuel cells that are differentiated by the type of electrolyte or the operating temperature. The type of electrolyte determines the operating temperature as the ions need to be mobile in the electrolyte. There are five types of fuel cells based on the type of electrolyte used

1. Alkaline fuel cell (AFC)
2. Polymer electrolyte membrane fuel cell (PEMFC)
3. Phosphoric acid fuel cell (PAFC)
4. Molten carbonate fuel cell (MCFC)
5. Solid-oxide fuel cell (SOFC)

Despite the differences in electrolyte and mobile ions, all fuel cells operate on the same electrochemical principle. They also differ in operating temperature ranges (from 60 to 1000 °C), fuel tolerance, performance characteristics, and materials used. The ionic charge carriers in PEMFC and PAFC - protons (H^+), SOFC - oxygen ions (O^{2-}), AFC - hydroxide ions (OH^-), and MCFC - carbonate ions (CO_3^{2-}). Detailed information about fuels, operating temperatures and mobile ions are shown in Figure 2.1.

The most commonly used fuel cell is the PEMFC, which operates at a relatively low temperature of about 80 °C. It uses H_2 free of CO as fuel and a Pt catalyst to accelerate the electrochemical reaction kinetics. Unlike the PEMFC, the SOFC operates at high temperatures, eliminating the need for an expensive catalyst while producing high-quality waste heat. It can also operate with almost any hydrocarbon fuel, such as biogas, liquefied petroleum gas, and compressed natural gas. Internal reforming of hydrocarbon fuels in the cell is possible in the SOFC. The co-production of heat and electricity makes it an attractive choice for residential and industrial applications. However, operation at high temperatures leads to slow start-up times compared to PEMFC [7]. In addition, the high operating temperature has a detrimental effect on the durability of the materials.

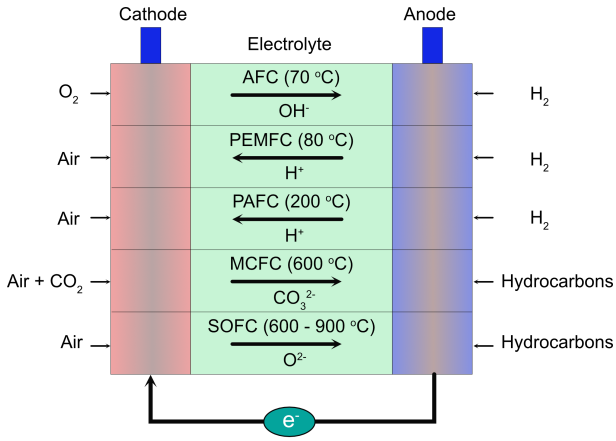

Figure 2.1: *Different fuel cell families. Adapted from [5]*

2.2 Solid oxide Fuel cell

The SOFC is based on an oxide ion conducting ceramic electrolyte combined with mixed conducting electrodes. To ensure the mobility of the oxygen ions, SOFC operate at high temperatures, which allows for fuel flexibility. The working principle of the SOFC using H_2 as fuel is illustrated in Figure 2.2a. A single SOFC cell is composed of three components: anode, cathode, and electrolyte. At the cathode, oxygen gas reacts to form oxide ions according to the reaction 2.2

$$\frac{1}{2}\, O_2 + 2e^- \rightarrow O^{2-} \tag{2.2}$$

The oxide ions migrate through the electrolyte and react with the fuel (H_2) at the anode electrode according to the reaction 2.3

$$H_2 + O^{2-} \rightarrow\ H_2O + 2e^- \tag{2.3}$$

The electrons released from reaction at anode flow through an external circuit. The overall reaction when hydrogen is used as fuel is same as Equation 2.1.

A single SOFC produces about 1 V at open-circuit voltage, depending on the fuel used. The cells are stacked together to produce usable power. The SOFC has a very high electrical efficiency at all capacities. This makes them suitable for small-scale applications such as powering homes, medium-scale applications such as airports, and large-scale power generation plants. Another advantage of the SOFC is that it can be used in a reverse mode as an solid oxide electrolyzer cell (SOEC), producing fuel from surplus electricity. SOECs coupled with renewable energy sources to produce hydrogen are a promising way forward for the sustainability of the hydrogen economy. The high temperature electrolyzer offers two key advantages. First, the thermal energy supplied is generally cheaper than electricity. Second, the low theoretical decomposition voltage makes electrolysis efficient at

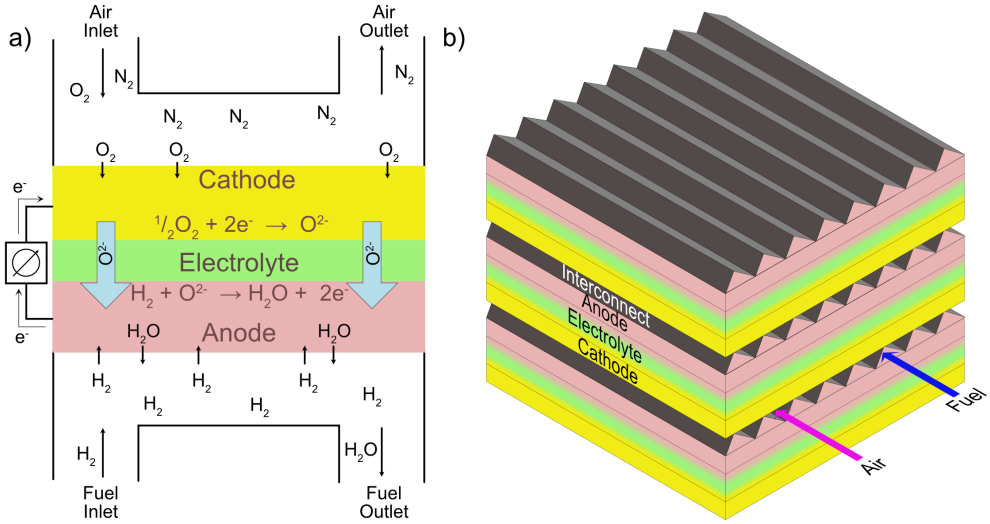

Figure 2.2: *Solid oxide fuel cell (a) Operating principle and (b) Fuel cell stack. Adapted from [8]*

high temperatures. Despite many advantages, the commercialization of SOFC is hindered by high costs and high degradation rates. In the following, the material requirements and the state of the art materials for different components of the SOFC are discussed.

2.2.1 Electrolyte

In SOFC, the basic requirements of the electrolyte materials are good ionic conductivity, low electrical conductivity, impermeability to gases, and stability in fuel and oxygen atmospheres [9]. The most commonly used electrolyte is zirconia (ZrO_2) doped with 8-10% yttria (Y_2O_3) (YSZ) [9, 10]. YSZ offers a good compromise between ionic properties, mechanical strength and conductivity. Cerium oxide (CeO_2) doped with about 20% gadolinium oxide (Gd_2O_3) (CGO) is a popular electrolyte with higher conductivity than YSZ and can therefore be used at lower operating temperatures. At the operating temperatures below 800°C, the conductivity of CGO is two orders of magnitude higher than that of YSZ [11]. The disadvantage of CGO is higher electronic conductivity at lower oxygen pressures (fuel side). Higher electronic conductivity leads to higher leakage currents, decreasing the power output [12].

2.2.2 Electrode Materials

Unlike the electrolyte, electrode materials must be porous, have good conductivity for ions and electrons, and be permeable to products and reactants. Since the electrochemical reactions in the SOFC occur at the electrodes, the electrode materials must have good catalytic properties to enhance the reaction rate and reduce polarization losses. The porous electrode creates a large surface area to maximize the contact area with the

reactant gases. High ionic and high electronic conductivity is achieved in many practical cases using composites containing two materials with either high ionic or high electronic conductivity. A common practice is to create a gradient of electrode and electrolyte material [12]. This also reduces the thermal stresses due to the differences in thermal expansion coefficient (TEC) of the electrodes and electrolyte.

2.2.2.1 Anode

The anode material should have high catalytic activity towards the electrochemical oxidation of fuel. Moreover, it must also be stable at the operating temperature over a wide range of p_{O_2} pressures. During operation, the p_{O_2} levels vary throughout the fuel cell due to increased H_2O at the fuel outlet [13]. The state of the art material for the anode is a porous cermet consisting of nickel and electrolyte material [12, 14]. The mixture ensures good adhesion and a similar TEC to other components. Since SOFC stacks are designed to use carbon-containing gases as fuels, the anode should have catalytic activity for water shift and reforming reactions.

2.2.2.2 Cathode

The cathode material should have high catalytic activity towards oxygen reduction reaction and be stable in oxidizing environments at high temperatures. Since the noble metals are excluded for economic reasons, the potential cathode materials are mixed oxides. The most commonly used cathode material is strontium doped lanthanum magnetite (LSM) [12]. The major limitation of LSM is the poor oxygen ion conductivity, resulting in a smaller triple-phase-boundary (TPB) area. This can be improved by the addition of YSZ [15]. Alternative materials such as strontium and iron-doped lanthanum cobaltite $La_{1-x}Sr_xCo_{1-y}Fe_yO_3$ (LSCF) have higher electronic conductivity which makes them promising for intermediate temperature SOFC [9].

2.2.3 Interconnect

A single solid oxide fuel cell (consisting of an anode, cathode, and electrolyte) typically provides an electric potential of less than 1V, depending on the cell efficiency and fuel utilization. To achieve higher voltages, multiple cells are electrically connected in series with the help of interconnects to form a fuel cell stack, as shown in Figure 2.2. The interconnects distribute the electrical current to the cells and separate the air atmosphere of one cell from the fuel atmosphere of the next cell. The basic requirements for the interconnect are similar to those for the electrolyte. However, the electrolyte is a good ion conductor and a poor electron conductor, while the interconnect must be a good electron conductor and a poor ion conductor. The main requirements of the interconnects [12, 16] are listed below:

- Stability at the operating temperature with air and fuel environment on either side for at least 80000 hours
- Similar TEC to the other cell components

- Good electrical conductivity and low ionic conductivity throughout the stack lifetime
- Chemical compatibility with other cell components.
- Impermeability towards gases
- Sufficient mechanical strength
- Ease of manufacturing

They should also be cheaper, as the cost is a major obstacle to the commercialization of SOFC.

2.2.3.1 Ceramic Interconnects

Traditionally, perovskite-type ceramics based on rare earth chromites such as CaO or SrO doped $LaCrO_3$ have been used to manufacture interconnects for operating temperatures above 1000 °C. High temperatures are required to achieve sufficiently high conductivity in perovskites. Ceramic materials offered high stability in fuel and air on either side and similar TEC to the other cell components. However, ceramic interconnects are expensive, difficult to fabricate, and less mechanically stable. In addition, the electrical and thermal conductivity of p-type semiconductors is much lower than that of metals [17]. Now a days, they are rarely used as interconnects in the fuel cell stack.

2.2.3.2 Metallic Interconnects

Recent improvements in the materials and manufacturing have allowed the operating temperature of SOFC to be lowered to the range of 600 - 900 °C. This, in turn, has enabled the use of metallic materials as interconnects. Compared to ceramic materials, metallic materials have higher mechanical strength, higher thermal and electrical conductivity, are easier to fabricate, and are less expensive. Among the potential candidates, chromia forming alloys show good oxidation resistance at high temperatures and good electrical conductivity of the oxide scale; thus have been extensively studied for use as SOFCs interconnects. Some notable challenges in using metallic materials as interconnects include high temperature corrosion in the air atmosphere, which is discussed in detail in section 4.1.

2.2.4 Balance of Plant

In addition to the SOFC stack, which constitutes of repeat units of anode, cathode, electrolyte, and interconnects, a wide range of auxiliary equipment supports the SOFC system, referred to as balance of plant (BOP). The balance of plant constitutes of cell frame, cathode preheater, heat exchangers, thermal management equipment, piping, pumps, fuel processors, exhaust burner, control systems, start-up heater, and power conditioner [3]. The cathodic preheater preheats the reactant gases to protect the ceramic stacks from thermal stresses due to rapid temperature changes. Heat exchangers recover high-quality thermal energy from the exhaust gas, and the exhaust burner burns the remaining fuel in the exhaust. Moreover, BOP in the SOFC system accounts for up to 75% of the total system manufacturing cost [3].

BOP components are subjected to harsh operating conditions. Therefore, ceramics are used to manufacture some of the BOP components [18]. However, the focus has shifted to metallic materials due to the decrease in the operating temperature. Metallic materials have higher strength, lower cost, and good fabricability compared to ceramic materials. They also reduce the material consumption and the weight of the SOFC system, which makes them attractive for mobile applications. However, the metallic materials used in the BOP are subjected to high temperature corrosion, which is discussed in section 4.2. Despite significant costs, research on BOP materials is very limited.

3 Corrosion of Steels

Corrosion is a gradual degradation of a material (usually metallic materials) by reaction with the environment. When exposed to conditions under which they are not thermodynamically stable, metallic materials convert to more stable forms such as oxides, hydroxides, or sulphides. Oxidation is a particular form of corrosion in which metals and alloys react with oxygen to form oxides, which is the focus of this work. The reaction between the metal (M) and the oxygen gas (O_2) is shown in Equation 3.1.

$$aM + \frac{b}{2}O_2 \rightarrow M_aO_b \tag{3.1}$$

Except for some noble metals, all other metals are thermodynamically unstable and form oxides when exposed to an oxygen containing atmosphere at ambient temperature. The reaction rates for oxide scale growth are low at ambient temperatures under dry conditions, so most metals do not appear to be affected by oxidation. However, the reaction rates are higher at higher temperatures so that they become problematic for the metallic materials used at high temperatures. The oxidation behaviour of the metal is influenced by thermodynamics and kinetics, which are discussed in the following sections.

3.1 Thermodynamics

Thermodynamics predicts the ability of a metal to form an oxide at a given temperature and under certain atmospheric conditions. The Gibbs free energy of a system, calculated using the Equation 3.2, helps determine the stability of the metal or oxide at constant temperature and pressure.

$$G = H - TS \tag{3.2}$$

Where G is Gibbs free energy, H is enthalpy, S is entropy and T is absolute temperature. The driving force for the Reaction 3.1 is related to the change in the Gibbs free energy associated with the conversion of metal to oxide. If the change in the Gibbs free energy (ΔG) is

- $\Delta G > 0$, the Reaction 3.1 is thermodynamically impossible.
- $\Delta G = 0$, the Reaction 3.1 is in equilibrium.
- $\Delta G < 0$, the Reaction 3.1 is spontaneous.

The change in Gibbs free energy ΔG for reaction 3.1 is shown in Equation 3.3.

$$\Delta G = \Delta G^o + RTln\frac{a_{M_aO_b}(s)}{a^a_{M(s)}a^{\frac{b}{2}}_{O_2(g)}} \tag{3.3}$$

where ΔG^o is the standard free energy change for the formation of M_aO_b, a_x is the activity of the products and reactants, R is the gas constant, and T is the absolute temperature. The activity of pure solids is 1, while the activity of gases is approximated to the partial pressure, $a_{O_2} = p_{O_2}$. At equilibrium $\Delta G = 0$, so the Equation 3.3 can be represented as Equation 3.4

$$\Delta G^o = RTln(p_{O_2}^{\frac{b}{2}}) \tag{3.4}$$

The equation 3.4 can be used to evaluate the stability of metals and oxides at a given temperature and oxygen partial pressure. The oxygen pressure at which the oxide is in equilibrium with the metal is called the dissociation pressure. The partial pressure of oxygen in the atmosphere should be higher than the dissociation pressure for oxidation to occur. The Ellingham diagram, shown in Figure 3.1, summarizes the standard free energies of oxide formation as a function of temperature for various metals. The nomographic scale on the right provides information about the partial pressure of oxygen required for oxidation to occur at a given temperature.

The Ellingham diagram can be used to compare the stability of different metals and oxides over a wide range of temperatures. The lower the line on the Ellingham diagram, the higher the stability of the oxide, and vice versa. Thermodynamics can only predict the existence of a phase at a given temperature and partial pressure under equilibrium conditions. However, the oxidation of metals depends on the kinetics, which will be discussed in the following section.

3.2 Kinetics

Oxidation kinetics is concerned with the evolution of the oxide scale over time. It is important in predicting the life of a component operating at high temperatures. The factors affecting the oxidation rate are temperature, oxygen pressure, pre-treatment of the metal, and the elapsed time of oxidation [20]. The most common method of studying oxidation kinetics is to monitor the change in mass with time. The mass of the metal increases as the metal absorbs oxygen from the atmosphere and forms an oxide. However, this method does not represent actual oxidation kinetics in the case of oxide spallation or oxide evaporation. Other methods to study oxidation kinetics include microscopy, chemical analysis of oxidized specimens and etc. [20].

The commonly encountered oxide growth mechanisms are linear, logarithmic, and parabolic, as shown in Figure 3.2. Oxidation often follows a combination of different rate equations. This could be because oxidation occurs either by two simultaneous mechanisms or because the rate-determining mechanism changes due to changes in the nature of the oxide scale.

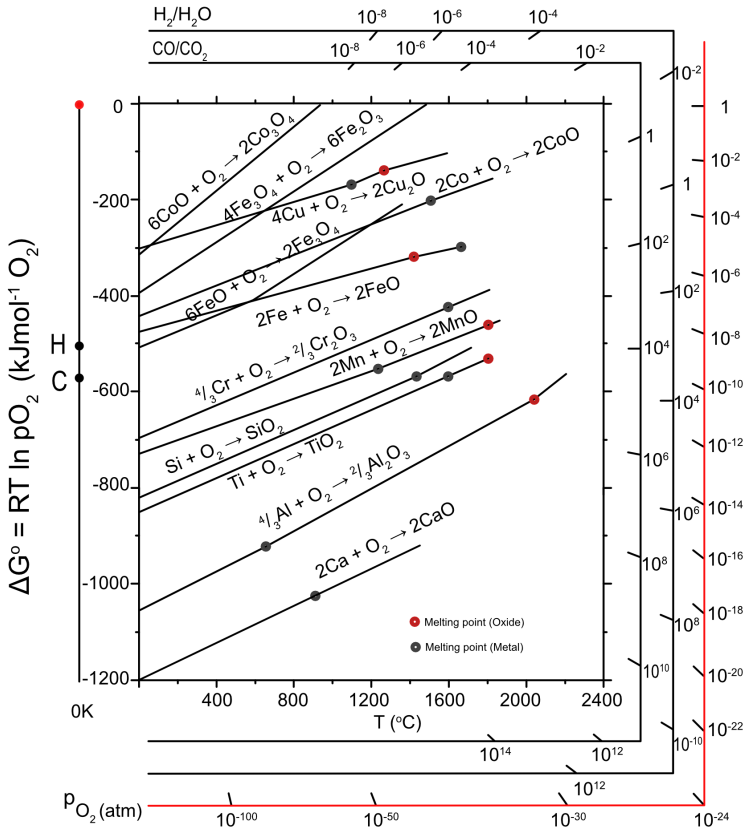

Figure 3.1: *Ellingham diagram for some metals and their metal oxides. Adapted from [19]*

3.2.1 Linear rate equation

Linear oxidation is described by the Equation 3.5.

$$\Delta m = kt + C \tag{3.5}$$

Where Δm is the mass change, k is the linear rate constant, and C is the integration constant. In linear oxidation, the oxidation rate is constant and is independent of the amount of metal or gas consumed. This means that the oxide scale is not protective. It is observed when the surface or phase boundary process or reaction is the rate-determining step [20].

3.2.2 Logarithmic rate equation

Logarithmic oxidation is described by the Equation 3.6

$$\Delta m = k_{log} log(t + t_o) + C \tag{3.6}$$

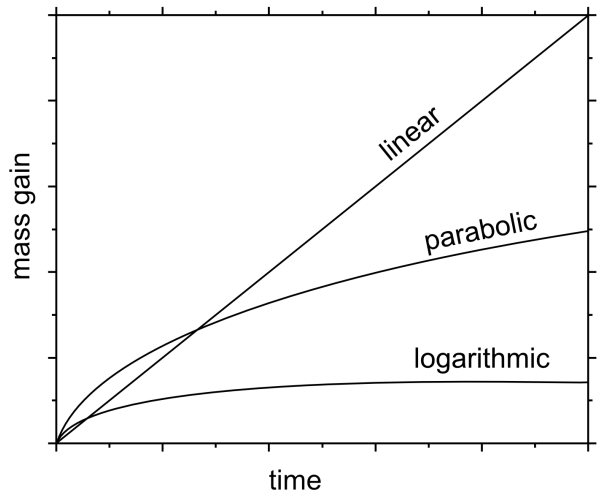

Figure 3.2: *The change of mass over time for three common oxide growth mechanisms. Adapted from [20].*

where Δm is the mass change, K_{log} is the logarithmic rate constant, t is the exposure time, and C is the integration constant. The reaction proceeds initially rapidly, followed by negligible rates. A large number of metals follow logarithmic oxidation in the temperature range of 300 - 400 °C and when the oxide scale is very thin [20]. There are several theories for the rate-determining step, such as chemisorption, transport of electrons and ions due to the electric field, but there is no general consensus [21].

3.2.3 Parabolic rate equation

Parabolic oxidation is described by the Equation 3.7

$$\Delta m^2 = k_p t + C \tag{3.7}$$

where Δm is the mass change, K_p is the parabolic rate constant, t is the exposure time, and C is the integration constant. Many metals follow parabolic oxidation at high temperatures. It can be explained based on a theory developed by Wagner in 1933. The main assumptions for this theory are that the oxide scale is dense and well adherent, the rate-determining step is the diffusion of ions through the oxide scale, the interfaces such as metal-oxide and oxide-gas are in thermodynamic equilibrium, and the oxygen solubility in the metal is negligible [22]. Since the rate-determining step is the diffusion of ions, the oxidation rate of metals following parabolic rate law decreases as the thickness of the oxide scale increases.

3.2.4 Breakaway oxidation

Breakaway oxidation is a mechanism in which the rate law changes from parabolic to linear oxidation. Breakdown of the protective oxide, which follows the parabolic rate

law, leads to rapid oxidation by the formation of non-protective oxide scales which follow the linear rate law. This can occur due to (a) mechanically induced chemical failure, e.g., when the oxide scale breaks or cracks due to growth stresses or thermal cycling, (b) intrinsic chemical failure, where the element forming the protective layer falls below a certain threshold and can no longer form a protective oxide [20].

3.3 Scale formation and growth

The formation of the initial oxide scale on a metal is a three-stage process, as illustrated in Figure 3.3. In the first stage, oxygen from the environment is adsorbed onto the metal surface. After charge transfer, the ions O^{2-} and M^{n+} are formed, creating an ionic bond between the ions. Subsequently, the metal oxide nucleates at the metal-gas interface and grows laterally to form a continuous scale. Both steps depend on surface orientation, crystal defects on the surface, surface preparation, and impurities in the metal and gas. Since the metal oxide separates the metal from the gas, the growth of the oxide scale in the third step occurs by solid-state diffusion of the metal ions and/or oxygen ions through the oxide scale. Typically, diffusion of both ions occurs simultaneously. Depending on the predominant diffusion process, the oxide scales can be classified into inward growing or outward growing oxide scales [20].

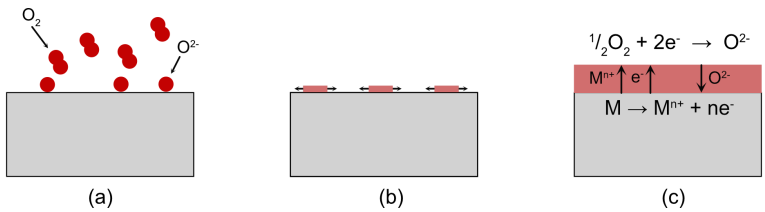

Figure 3.3: *Schematic illustration of oxide growth in three steps (a) adsorption (b) oxide nucleation and (c) oxide scale growth. Adapted from [20]*

If the diffusion of ions is the rate-determining step in a oxidation reaction, then the rate of oxidation decreases as the oxide scale becomes thicker. Such oxide scales, which are dense and have low ion diffusivity, are called protective oxides. However, if the oxide scale is porous, then the gas transport through the oxide scale is easier, resulting in a higher oxidation rate, called as non-protective oxide scale.

3.4 Oxide evaporation

Some oxides such as Cr_2O_3, WO_3, and MoO_3 react with the environment to form volatile metal oxide species [23, 24]. The oxide evaporation reaction has high activation energy; therefore, the oxide evaporation is more relevant at high temperatures [20, 21]. The evaporation of the protective scale leads to accelerated consumption of the protective scale

forming element in the alloy. Chromia forming alloys that form a protective Cr_2O_3 layer are used extensively for high temperature applications. However, chromium evaporation limits the applicability of chromia forming alloys at high temperatures and is extensively studied in the literature [20, 25, 26, 27]. Chromium evaporation causes cathode poisoning in the SOFC (see section 4.1). The mechanism of chromium evaporation is relevant for this work and discussed below.

Chromium oxide is unstable thermodynamically at high temperatures in environments containing O_2 or $O_2 + H_2O$. Chromium oxide reacts with O_2 predominantly at temperatures above 1000 °C, to form CrO_3, as shown in Equation 3.8. In the presence of H_2O, the chromium evaporation proceeds at relatively lower temperatures to form $CrO_2(OH)_2$, $CrO_2(OH)$ as shown in the Equation 3.9, 3.10. From theoretical and experimental evaluations, it is concluded that $CrO_2(OH)_2$ is the major volatile compound at temperatures below 900 °C [23, 28, 29]. The chromium evaporation is affected by various factors such as temperature, humidity, gas flow, and the orientation of the sample to the flow.

$$Cr_2O_3(g) + \frac{3}{2}O_2(g) \rightarrow 2CrO_3(g) \tag{3.8}$$

$$Cr_2O_3(s) + \frac{3}{2}O_2(g) + 2H_2O(g) \rightarrow 2CrO_2(OH)_2(g) \tag{3.9}$$

$$Cr_2O_3(s) + O_2(g) + H_2O(g) \rightarrow 2CrO_2(OH)(g) \tag{3.10}$$

Mass gain data helps predict the oxidation kinetics; thus, the life of metallic material exposed to high temperatures. However, with simultaneous oxidation and chromium evaporation, chromium consumption in the alloy is higher than indicated by the mass gain measurements. In addition, chromium evaporation results in a thinner oxide scale, resulting in a higher oxidation rate. Chromium depletion due to chromium evaporation can result in breakaway oxidation.

3.4.1 Paralinear oxidation

When a chromia forming alloy is exposed to an environment containing $O_2 + H_2O$ at high temperatures, oxidation and oxide evaporation occur simultaneously. Oxidation leads to the growth of the oxide scale, while evaporation leads to the loss of the oxide scale. Initially, the oxide scale grows faster than the oxide scale lost due to chromium evaporation, resulting in a positive net mass gain. As the oxide scale becomes thicker, the oxidation rate decreases. At some elapsed time, the oxide scale growth due to oxidation equals to the oxide scale lost to chromium evaporation, at which point the critical thickness of the oxide scale is reached [30]. Once the critical thickness of the oxide scale is reached, mass loss is observed due to the continuous loss of Cr species by evaporation. The oxidation phenomenon with a combination of parabolic oxidation and linear evaporation is called paralinear oxidation, as shown in Figure 3.4 [30, 31].

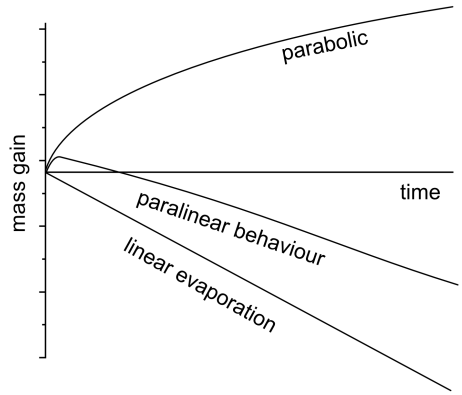

Figure 3.4: *Paralinear oxidation behaviour which is the combination of parabolic mass gain and linear mass loss. Adapted from [30, 32]*

4 Challenges with metallic materials in SOFC

Since the operating temperature of SOFC is in the range of 600 - 900 °C, metallic materials used in SOFC face challenges due to high temperature corrosion. Metallic materials exposed to high temperatures in air rely on the formation of a passivating oxide layer that retards the oxidation of the material. This oxide layer protects the metallic material from further corrosion. Alloys capable of forming adherent scales of either SiO_2, Al_2O_3 or Cr_2O_3 are usually preferred for high temperature applications. SiO_2 and Al_2O_3 are slow-growing oxide scales compared to Cr_2O_3 scale. To ensure long operating lifetimes for the SOFC system, the metallic materials used must have good resistance to high temperature corrosion. Nevertheless, other factors such as strength, design constraints, application, temperature, and cost also play an important role in material selection. This chapter explores the challenges of using metallic materials in SOFC interconnect and the balance of plant components.

4.1 Interconnect steels

The functions and requirements for the interconnect steels used are described in the section 2.2.3. Metallic interconnects have replaced the traditional ceramic interconnects in the SOFC's which operate in the range of 600 - 900 °C. As the interconnects are used to electrically connect the individual cells, growth of the oxide scale on the interconnect will lead to an increase in the electrical resistance across the cell, which reduces the performance of SOFC. Although SiO_2 and Al_2O_3 oxide scales have excellent oxidation resistance, the electrical conductivity of these scales is extremely low, making them unsuitable for interconnect applications. Cr_2O_3 is a semiconductor in the operating temperature range of SOFC, and has better conductivity than SiO_2 and Al_2O_3 [20]. Cr_2O_3-forming alloys exhibit a good compromise between high temperature oxidation resistance and oxide scale electrical conductivity. Thus, they have been extensively investigated for use as SOFC interconnects.

4.1.1 Material Selection

There are several commercial chromia forming alloys such as ferritic stainless steels (FSS), austenitic stainless steels, Cr-base alloys, and Ni-base alloys. Of these, Ni-base alloys are considered as the best performers at high temperatures [33]. Nevertheless, only ferritic stainless steels and Cr-base alloys are considered for interconnect application as their TEC matches well with the other cell components. Cr-base alloys such as Plansee Ducrolloy ($Cr_5Fe_1Y_2O_3$) were favoured early on as substitutes for ceramic interconnects because of their excellent corrosion and electrical properties [34]. However, ferritic stainless steels have replaced the Cr base alloys to be used in interconnects because they are easier to manufacture and less expensive. Ferritic stainless steels have a body-centred cubic crystal. The TEC of ferrites ranges from 11.5 * $10^{-6}K^{-1}$ to 14 * $10^{-6}K^{-1}$ which is

similar to the other ceramic components in the SOFC (TEC = 10.5 - 12.5 * $10^{-6}K^{-1}$) [35]. As a result, FSS with Cr content between 16 – 23 wt% are extensively studied for large scale manufacturing of interconnects [36].

Despite the advantages of using FSS - such as similar TEC, high electrical and thermal conductivity, ease of formability, and lower cost - over ceramics for interconnect applications, they have certain issues that impact the long-term operation of SOFC stacks:

- The operation of FSS at high temperatures results in the growth of chromia scale on the surface of the interconnect, increasing the electrical resistance across the cell, deteriorating the cell performance. Thicker chromia scales might also lead to scale spallation, losing the electrical contact with the electrodes.
- In the cathode atmosphere, chromia scale reacts with oxygen in the presence of water vapour to form volatile Cr (VI) species such as CrO_3 and $CrO_2(OH)_2$, as shown in section 3.4. These volatile species react with the cathode and get deposited at the active triple-phase boundaries, hindering the oxygen reduction reaction. This will result in reduced electrochemical activity of the cathode and thereby degrades SOFC performance over time, also known as chromium poisoning [37].
- Chromium evaporation also leads to Cr depletion in the steel. Breakaway corrosion occurs when the chromium content in the steel falls below a certain threshold, resulting in rapid degradation of the fuel cell.

4.1.1.1 Alloying elements

In addition to iron and chromium, ferritic stainless steels contain minor alloying elements that are either intentionally added or remnants from the steel making process that are expensive to remove. Some minor alloying elements in ferritic steels significantly influence the degradation mechanisms.

Manganese

Manganese is an important minor alloying element present in all FSS considered for the interconnect application. Upon oxidation, Mn diffuses through the chromia scale to form $(Cr, Mn)_3O_4$ spinel on the chromia scale, decreasing the chromium evaporation and improving the conductivity. Several authors showed that $(Cr, Mn)_3O_4$ spinel reduces the chromium evaporation by a factor of 2 to 3 compared to the Cr_2O_3 scale at 800 °C [25, 38]. However, chromium evaporation is still high for the long-term operation of the SOFC. The conductivity of $(Cr, Mn)_3O_4$ spinel is reported to be at least an order of magnitude higher than that of Cr_2O_3 [39, 40].

Silicon and Aluminium

Silicon and aluminium are the remnants of steel production, where they are used as deoxidizers [41]. Si and Al require a lower oxygen partial pressure than Cr and are therefore oxidized internally in the alloy. If they are present above a certain threshold, subscales such as SiO_2 and Al_2O_3 are formed, which results in two issues. First, the

electrically insulating oxides increase the electrical resistance across the cell [42, 43, 44]. Moreover, the SiO_2 subscale is reported to reduce the adhesion between the oxide scale and metal due to the dissimilar TEC between the alloy and SiO_2[26, 45]. Removal of Si and Al from steel requires vacuum induction melting, which results in additional costs to the manufacturing process.

Refractory elements
Refractory elements such as Nb, W, Mo are added to form laves phases such as (e.g., $(Fe, Cr)_2(Nb, W, Mo)$). Laves phases are reported to bind Si and hamper the formation of SiO_2 [42]. Moreover, the laves phases increase the hardness and creep resistance of the steel by hindering dislocation motion [43]. However, increasing the Nb content is reported to increase the oxidation rate of FSS due to the doping of Cr_2O_3[43].

Reactive elements
The beneficial effects of minor addition of reactive elements (RE) belonging to the rare earth elements such as Zr, Ce, Hf, La on high temperature oxidation are well established in the literature, known as the reactive element effect [46, 47, 48, 49]. The most common effects of the reactive elements are

- Decrease in the oxidation rate of the material.
- Improvement in scale adhesion and resistance to spallation.
- Modification of the oxide scale microstructure.
- Selective oxidation of the alloys.
- Change in the growth mechanism of the oxide scale.

The effects mentioned above are visible already at the tiny addition (0.1% La) of reactive elements. The mechanism of the reactive elements is not yet fully understood. The most prominent hypothesis is that RE changes the growth mechanism of the oxide scale. Undoped Cr_2O_3 scale grows predominantly by the outward diffusion of metal cations. In the Cr_2O_3 scale doped with RE, the outward diffusion of the metal cations is inhibited by the RE segregated at the oxide grain boundaries. As the smaller oxygen anions are not affected, the growth of the chromia scale changes from predominantly outward migration of chromium ions to inward diffusion of oxygen ions [50, 51, 52]. The change in diffusion mechanism results in lower oxidation and also an increase in scale adhesion. The improvement in the electrical properties of the oxide scale doped with reactive elements is observed [53, 54, 55].

Reactive elements can be added to the steel melt during the production; such is the case for Crofer 22 APU, Crofer 22 H, and Sanergy HT. However, the addition of RE during the steel production increases the overall manufacturing cost, making these steels expensive. Other methods of applying the reactive elements are the dispersion of RE oxides and coating the surface with a thin layer [54, 56]. More detailed information on reactive elements can be found in [52, 57, 58, 59]

4.1.1.2 Tailor-made steels

Tailor-made steels are developed by adding and removing certain minor alloying elements to improve the performance and mitigate interconnect degradation, thus ensuring long-term operation. The widespread commercially available tailor-made steels towards interconnect material are Crofer 22 APU, Crofer 22 H, Sanergy HT, and ZMG232 G10. The common features in these steels are (i) High Cr content (approximately 22%) to ensure the formation of chromia scale during the long-term operation. Further increasing the Cr content leads to undesirable brittle sigma phase formation. (ii) Minor addition of Mn ($<$ 1 wt%) to form $(Cr, Mn)_3O_4$ spinel on the chromia scale, reducing the chromium evaporation. (iii) Addition of reactive elements such as La, Ce to improve the oxidation kinetics and scale adhesion. (iv) Reducing the SiO_2 subscale formation by containing a low Si content in the alloy as in Crofer 22 APU and ZMG232 G10 or by addition of refractory elements to bind Si as in Crofer 22H and Sanergy HT.

Despite the improved performance of tailor-made steels, they still exhibit high chromium evaporation and chromia scale growth. Moreover, the addition of reactive elements and other stringent requirements combined with low production volumes make these steels expensive. Interconnects contribute a significant part of the total raw material cost in a SOFC stack [3]. Therefore, a strong incentive exists to reduce the cost of the interconnects, which reduces the overall cost of the SOFC stack. Replacing the tailor-made steels with widely available low-cost ferritic stainless steels such as AISI 441, AISI 444, and AISI 430 would decrease the interconnect cost. The above-mentioned low-cost commercial Fss mentioned above have approximately 16 – 19% Cr, 0.3 to 0.6% Mn and minor alloying elements such as Nb, Ti, Mo and W. The main disadvantages of using commercial FSS are the lower Cr content and the formation of the SiO_2 subscale. Thus, these steels are mainly explored for intermediate temperature SOFC's with an operating temperature below 750 °C.

4.1.2 Protective coatings

Despite the advances in adapting steel chemistry targeted towards SOFC interconnect, the high oxidation rate and chromium evaporation makes it impractical to use uncoated FSS as an interconnect material. To remain competitive in the market, SOFC needs to have a service life of up to 80000 hours [60]. Protective coatings are an alternative approach to the bulk modification of alloys, in which a metallic interconnect surface is modified by a protective and conductive layer. Diffusion barrier coatings are proven to be effective in reducing chromium evaporation and chromia scale growth [61, 62, 63].

The requirements for coatings are similar to those for interconnects like TEC identical to other cell components, good electrical and thermal conductivity, ease of manufacturing, chemical compatibility with adjacent cell components, good adhesion and lower cost. Moreover, they should be effective in mitigating chromium evaporation and oxide scale growth. Interconnect coatings can be broadly divided into two groups, spinel coatings and perovskite coatings.

Perovskite coatings

The general formula of the perovskite structure is ABO_3, where A sites are occupied by low valance cations such as La, Sr, Ca and Pb, while the B sites are occupied by higher valance transition metal cations such as Ti, Co, Fe, etc. Perovskite coatings exhibit p-type electronic conduction in an oxidizing environment and are stable under low oxygen partial pressures [61, 64]. The most common perovskite coatings researched for the interconnect application are lanthanum chromite ($LaCrO_3$), lanthanum strontium chromite ($La_{1-x}Sr_xCrO_3$), lanthanum strontium manganite ($La_{1-x}Sr_xMnO_3$), lanthanum strontium cobaltite ($La_{1-x}Sr_xCoO_3$) and lanthanum strontium ferrite ($La_{1-x}Sr_xFeO_3$) which were prepared by radio-frequency magnetron sputtering, sol-gel and screen printing [62]. They have high electronic conductivity, similar TEC to the other ceramic components. However, thicker coatings are required to decrease the oxidation rate, and the coatings often have poor adhesion to the substrate [61]. Despite the improvements, ionically conductive perovskites remain an ineffective barrier to volatile Cr species or oxygen diffusion [25, 63, 65].

Spinel coatings

Spinels are oxide materials with the general formula AB_2O_4, where A and B are divalent, trivalent, and quadrivalent cations occupying octahedral and tetrahedral sites in the face-centred cubic oxygen anion lattice [62]. The properties of the spinels, such as conductivity, thermal and electrical properties, and TEC can be tailored by adjusting the choice and ratio of A and B cations. They have attracted attention because of their ability to suppress chromium evaporation. Detailed thermal and electrical properties of various spinels can be found in [66].

Mn-Co spinel oxide (MCO) coatings are extensively researched for the interconnect application. They are considered promising on the air side of the interconnect as they have demonstrated to reduce chromium evaporation and area-specific resistance across the interconnect [67, 68, 69]. $(Co, Mn)_3O_4$ spinel has a conductivity of 6.4 – 60 $S.cm^{-1}$ at 800 °C and TEC in the range of 11.5 - 14.4 * $10^{-6}K^{-1}$ between 25°C- 800°C [66]. Several attempts to improve the conductivity of the $(Co, Mn)_3O_4$ spinel by doping with Co, Cu, and Fe have been reported [62, 63, 70]. These coatings can be deposited using various techniques such as sol-gel dip coating, electrophoretic deposition, electroplating, physical vapour deposition, atmospheric plasma spray coating and screen printing. Physical vapour deposition (PVD) coatings are particularly suitable because they can be applied in roll to roll in a high-volume process efficiently, resulting in lower cost [71]. $(Co, Mn)_3O_4$ spinel coating on the steel can be achieved by depositing metallic Co, which oxidize during the high temperature exposure to form Co_3O_4 spinel. Subsequent outward diffusion of Mn from the steel results in the formation of $(Co, Mn)_3O_4$ spinel [69].

Reactive element coatings

Reactive element coatings are proposed for the interconnect application. Even a very thin coating of reactive elements has shown a beneficial effect on the corrosion behaviour of the alloy [55, 72, 73]. Moreover, Fontana et al.[55] showed improvement in the oxidation behaviour and oxide scale adhesion of reactive element oxide (La_2O_3, Nd_2O_3 and Y_2O_3)

coated chromia forming steels such as Crofer 22 APU, AL 453 and Haynes 230. However, reactive element coating is ineffective in preventing chromium evaporation [56].

Spinel coating and the reactive element coating can be combined to achieve lower chromium evaporation and improve oxidation resistance. Several authors reported the improved behaviour of MCO coatings by the addition of reactive elements [74, 75, 76, 77, 78]. Ce/Co coatings are considered state-of-the-art coatings that combine the positive effects of both the MCO coating and a reactive element coating. A 10 nm Ce and a 600 nm thick Co on the top deposited using PVD are extensively researched for interconnect application [53, 56, 74, 79, 80, 81]. Moreover, the self-healing properties of these coatings allow steel sheets to be shaped to interconnect after coating, which is highly cost-effective [82].

4.1.3 Electrical Conductivity of Oxide Scales

The main function of the interconnect is to conduct electrons, thereby electrically connecting the fuel cells in the fuel cell stack. The main challenge for the electrical conductivity of the interconnect is the formation of oxide scale during high temperature operation. The conductivity of the oxide scale is several orders of magnitude lower than the steel. Therefore, the oxide scale growth increases the overall resistance of the steel, decreasing the efficiency of the fuel cell. The degradation can be experimentally evaluated using the area specific resistance (ASR).

The electrical conductivity of a material can be defined using the Equation 4.1

$$\sigma = \sum \mu_i * n_i * q_i \tag{4.1}$$

Where μ_i is the mobility, n_i is the number and the q_i is the charge of carrier i. In oxides, the charge carriers are electrons, electron holes, ions, or ion holes. Thus, the conductivity for the oxides can be defined as the sum of electronic and ionic charge carriers as shown in Equation 4.2

$$\sigma = \sigma_{electronic} + \sigma_{ionic} \tag{4.2}$$

The mobility μ_i of electrons decreases, and mobility μ_i of ions increases with the temperature. The charge carrier concentration n_i increases with the temperature. In oxides, the increased charge carrier concentration and mobility of ions supersedes the decreased mobility of electrons; therefore, the conductivity of oxides increases at higher temperatures. In the case of metals, the decreased mobility of electrons supersedes the increased charge carrier concentration, resulting in a decrease in conductivity [20]. The temperature dependence of the electrical conductivity of the oxide scale is defined using Arrhenius relation in Equation 4.3

$$\sigma = \sigma_o * exp\left(\frac{-E_a}{R * T}\right) \tag{4.3}$$

where σ_o is the pre-exponential factor, E_a is the activation energy, R is the ideal gas constant and T is the temperature.

The ASR is commonly used to describe the electrical behaviour of the interconnect, which is independent of the area, as shown in the equation 4.4

$$ASR = A * R_e = A * \frac{1}{\sigma} * \frac{L}{A} = \frac{L}{\sigma} \tag{4.4}$$

where R_e is the resistance, σ is the conductivity, L is the oxide thickness and A is the measured area.

Conductivity of Chromia
The electrical properties of the interconnect are mostly dependent on the chromia scale growth. Chromia scale is considered an intrinsic semiconductor at temperatures above 1000 °C [83] and a extrinsic semiconductor at temperatures below 1000 °C [84]. Thus, electronic conductivity of the chromia scale below 1000 °C depends on the partial pressure and is dominated by dopants and impurities. Depending on the dopant and the oxygen partial pressure, the doped chromia shows either p-type semiconductor behaviour or n-type semiconductor behaviour. Since the partial pressure of oxygen varies through the oxide scale, some researchers reported the presence of both n-type and p-type behaviour in the chromia scale [85, 86]. The thermally grown chromia scale is doped by several alloying elements such as Ti, Ni, Fe, Mn, and Nb present in the steel [84, 87, 88]. Usually, the conductivity of the oxide scale is improved by the dopants [87, 89]. Thus, the electrical conductivity of the chromia scale is reported to vary between 0.001 and 0.05 Scm^{-1} at 800 °C [84, 90, 91, 92].

Conductivity of Spinels
Spinel coatings are extensively used to reduce chromium evaporation, as discussed in section 4.1.2. Since the coatings are inevitable, it is important to understand the electrical properties of various spinels proposed as interconnect coatings. Spinels are believed to conduct electrons via a hopping mechanism between the octahedral sites [93]. To be a good electronic conductor, spinels should be able to accommodate different valence electrons at the octahedral states. The $(Cr, Mn)_3O_4$ spinel has higher conductivity than the Cr_2O_3 scale [39, 40], but much lower conductivity than $(Co, Mn)_3O_4$ spinel [66, 94, 95]. This is because of the presence of Cr, which has only one stable oxidation state Cr^{+3} and a strong preference to occupy the octahedral sites [66, 96]. An extensive list of the conductivity and thermal expansion of various spinels at 800 °C can be found [66]. Based on that study, $(Co, Mn)_3O_4$ and $(Cu, Mn)_3O_4$ spinels are best suited for the interconnect coating. However, Göebel et al. [97] showed the minimal influence of the coating conductivity on the ASR since the conductivity of the coating is several orders of magnitude higher than the chromia scale.

4.2 BOP Materials

BOP components are exposed to various temperatures and atmospheres depending on their location, function, and contact with the exhaust. The use of chromia forming materials in BOP causes problems similar to those encountered with the interconnects,

such as chromium evaporation. BOP components located upstream of the fuel cell can be a significant source of volatile $Cr(VI)$ species [98]. However, unlike the metallic interconnects, which have attracted considerable attention from researchers worldwide, materials for BOP components are often overlooked. Coatings designed to circumvent the drawbacks of metallic interconnects are difficult to implement on BOP components due to the complex geometries of the components.

The metallic materials used for BOP components should have good oxidation resistance, lower cost, and are readily available. Moreover, they should have good mechanical properties, good machinability, high thermal conductivity, and long-term creep behaviour. Unlike the materials for interconnects, there are no restrictions on the conductivity of the scale for the BOP components. Hence, Al_2O_3 oxide forming alloys can be used for this application. With nominal restrictions on the TEC, austenitic steels and Ni-based alloys can be explored for the BOP application.

5 Experimental Setup and Methods

5.1 Investigated Materials

5.1.1 Balance of Plant

Five alloys from four material groups are investigated for their application in the balance of plant components. The chemical composition of the selected alloys is shown in Table 5.1. The DIN number, material group, and the commercial names of the alloys used in this thesis are listed in Table 5.2. The alloys with a thickness of 0.5 mm were cut to 17 mm x 15 mm coupons and exposed without further surface treatment. A197 was obtained as a 2 mm thick sheet cut into square coupons (15 mm x 15 mm x 2 mm) and ground to 0.5 mm using SiC paper to a grit #1200 finish. The coupons were exposed at 650 °C and 850 °C for 500 h. One set of coupons were pre-oxidized at 900 °C for 24 h before exposure at 650 °C for 500 h.

Table 5.1: Chemical composition of the selected materials in weight %.

Alloy	C	Si	Mn	Cr	Ni	Al	Nb	Fe	Mo	Ti
AISI 441	0.02	0.58	0.42	17.53	0.28	-	0.39	Bal		0.164
AISI 444	0.01	0.37	0.3	18.92	-	-	0.56	Bal	1.85	0.003
Alloy 600	0.02	0.18	0.24	16.25	74.19	0.22	0.08	7.93	-	0.29
Alloy 800H	0.07	0.4	0.6	20.8	30.4	0.28	-	Bal	-	0.3
A197	0.02	1.25	0.1	12.4	-	3.7	-	Bal	Reactive Elements	

Table 5.2: Details of the materials from Table 5.1

Alloy	DIN	Commercial name	Material group	Thickness
AISI 441	1.4509	-	FSS	0.5 mm
AISI 444	1.4521	K44M	FSS	0.5 mm
Alloy 600	2.4816	-	Ni-base alloy	0.5 mm
Alloy 800H	1.4958		Austenitic stainless steel	0.5 mm
A197		Kanthal® EF101	Alumina forming FSS	2 mm

5.1.2 Interconnects

Three FSS with a thickness of 0.3 mm were selected for the interconnect application. Of these, 441 and 444 are commercial FSS, while Crofer 22 APU is the tailor-made FSS for the interconnect application. The chemical composition of the investigated steels is shown in Table 5.1. In papers II, III uncoated steels are compared with the coated steel. Two types of coupons from steel sheet and pre-cut steel, shown in Figure 5.1, are used for the exposures. In the pre-cut steel, coupons of size 17 mm x 15 mm were etched on the steel sheet and are attached to the remaining material with two 1 mm wide sections. Coatings are deposited on pre-cut steel and steel sheet using a proprietary

physical vapour deposition process at Sandvik Materials Technology [71]. The coatings deposited on various substrates are listed in Table 5.4. The coated steel sheet was further cut into 17 mm x 15 mm coupons, which are referred to as sheet-coated. The coupons from the coated pre-cut steel sheet are referred to as precut-coated. All the exposures on the uncoated steels were performed on coupons from pre-cut steels.

Table 5.3: Chemical composition of the selected steels in weight %.

Alloy	Fe	Cr	C	Mn	Si	Cu	Ti	Nb	Mo	RE
Crofer 22 APU	Bal	22.92	0.004	0.38	0.01	0.01	0.06	-	-	0.07
AISI 444	Bal	19.03	0.015	0.35	0.40	-	0.005	0.6	1.86	-
AISI 441	Bal	17.56	0.014	0.35	0.59	-	0.17	0.39	-	-

Table 5.4: Details of the coating-steel combinations used in the thesis.

Alloy	DIN	10Ce 600Co	20Ce 600Co	50Ce 600Co
AISI 441	1.4509	✓	✓	✓
AISI 444	1.4521	✓		
Crofer 22 APU	1.4760	✓		

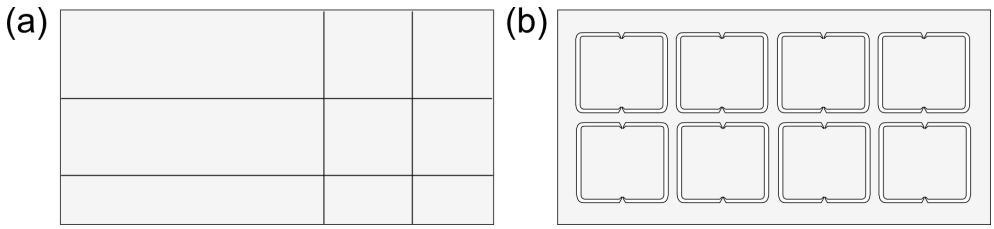

Figure 5.1: *Steel used for coating (a) sheet (b) pre-cut steel with coupon dimensions 17 mm x 15 mm.*

5.2 Exposure

All exposures were carried out in tubular furnaces with a horizontal quartz tube reactor, as shown in Figure 5.2. The exposures were performed in continuous airflow, saturated with 3% H_2O to represent the airside of SOFC. 3% H_2O in the air was obtained by flowing the air through a heated water bath connected to a condenser set at 24.4 °C. The water vapour in the air was measured using Michell Instruments Optidew Vision™ chilled mirror humidity sensor. To achieve a flow independent regime, the airflow was set at 6000 $sml\ min^{-1}$, which corresponds to a linear velocity of 27 cm/s. A flow restrictor was placed in front of the coupons to minimize natural convection and ensure a more uniform flow pattern. All coupons were degreased and cleaned with acetone and ethanol in an ultrasonic bath at room temperature before the exposure. Three identical coupons were

used for each exposure. The coupons were mounted on an alumina holder positioned parallel to the airflow.

5.2.1 Mass Gains

The oxidation kinetics of the exposed alloys are studied using discontinuous mass gain measurements. The coupons were removed from the furnace at regular intervals and allowed to cool down to room temperature. The mass of the coupons is recorded using an XP6 scale (Mettler Toledo). After recording the mass, the samples were reheated to the same temperature as before. The mass gains from the discontinuous mass gain measurements are compared to the mass gains recorded after continuous chromium evaporation measurements.

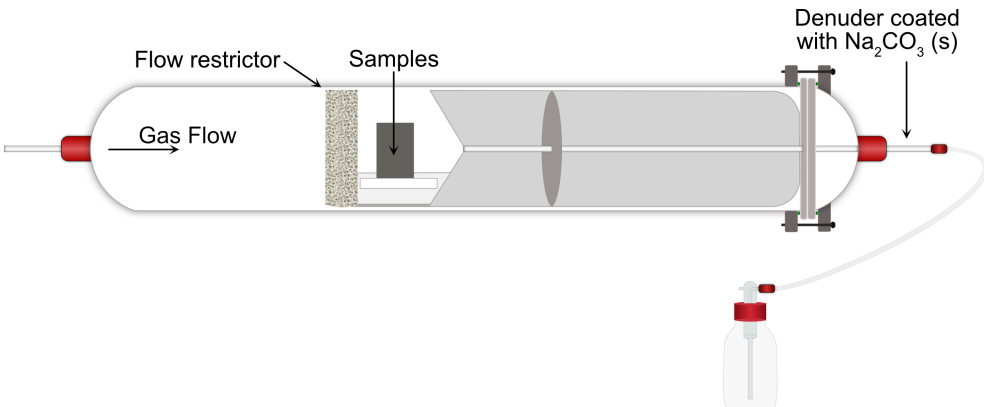

Figure 5.2: *Schematic illustration of the experimental setup [99]*

5.2.2 Denuder Technique

The time-resolved in-situ chromium evaporation measurements were performed using the Denuder technique. A denuder tube coated with Na_2CO_3 was placed at the outlet of the reactor as shown in Figure 5.2. The downstream of the gas was directed through a denuder tube coated with Na_2CO_3. The volatile Cr species formed according to the Equation 3.9 react with Na_2CO_3 as shown in the Equation 5.1.

$$Na_2CO_3(s) + CrO_2(OH)_2(g) \rightarrow Na_2CrO_4(s) + H_2O(g) + CO_2(g) \tag{5.1}$$

The end of the denuder was connected to a wash bottle to collect any detached flakes of Na_2CrO_4. The denuders and wash bottles were replaced at regular intervals. The removed denuders and wash bottles were leached with distilled water. The chromium species were quantified with an Evolution 60s Thermo Scientific spectrophotometer.

5.3 Analytical Techniques

5.3.1 Spectrophotometry

Spectrophotometry is an analytical method for quantifying light-absorbing ions or molecules in a solution. Each chemical compound absorbs light in a certain range of wavelengths. The absorption of light increases with the increase in the concentration of the substance. The absorbance can be measured using the Beer-Lambert law [100] as shown in Equation 5.2:

$$A = log_{10}\frac{I_0}{I} = \varepsilon_\lambda.c.l \tag{5.2}$$

Where A is the absorbance, I_0 is the intensity of transmitted light for a given wavelength using pure solvent, and I is the intensity of transmitted light through the solution, ε_λ is the molar absorptivity, l is the path length of the light through the solution, and c is the concentration. The maximum light absorbance for chromate in water solution is at a wavelength of 370 nm. The monochromatic light at this wavelength is used for all concentration measurements. Fournier-Salaün et al. [101] reported that the pH of 9 and above is required for almost 100% chromate predominance in the solution. The solutions leached from denuders and wash bottles are tested for pH and usually are alkaline with pH > 9. In other cases, 0.1 M $NaOH$ was added to the solution.

5.3.2 Broad ion beam

A Broad ion Beam Milling System Leica EM TIC 3X equipped with three Ar ion guns was used for polishing the cross-sections of the coupons. A broad ion beam (BIB), typically of Ar ions, is used to bombard a target material, sputtering the atoms from the surface of the target. Since the milling takes place over a wide area, finely polished cross-sections in the millimetre range are obtained for further analysis. The main advantage of using BIB over mechanical polishing is that BIB is a dry process and produces smoother surfaces revealing microstructural features.

5.3.3 Scanning Electron Microscope

A scanning electron microscope (SEM) is an electron microscope that scans the surface with a focused beam of electrons to produce images. As a result, SEM has a much higher resolution compared to the optical microscopes which uses visible light. The electron source emits electrons that are accelerated and passed through a system of magnetic lenses and apertures to produce a focused beam of electrons that hits the surface of the sample. The electrons interact with atoms in the material, producing various signals such as secondary electrons, Auger electrons, back-scattered electrons, and X-ray emissions. These emissions are transformed into signals containing information about the topography, orientation, and composition of the material with the help of suitable detectors [102]. Figure 5.3 shows the interaction volume and different types of emissions from the electron material interactions. The SEM used for the work in this thesis is a JEOL JSM-7800F Prime SEM, equipped with an Oxford Instruments Energy Dispersive X-ray spectrometer

(EDS). Secondary electrons and back-scattered electrons are used for imaging, and X-ray emissions are used to analyze the composition of the investigated samples.

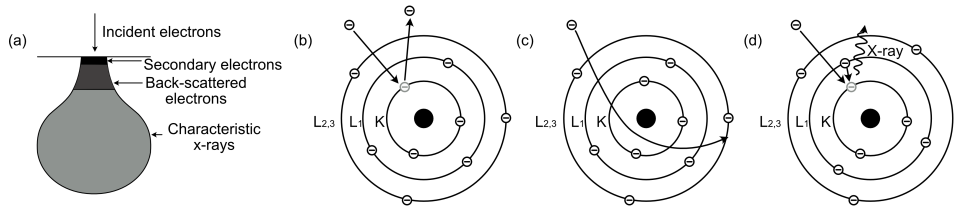

Figure 5.3: *Schematic illustration showing the (a) interaction volume (b) secondary electrons (c) back scattered electrons (d) characteristic x-ray. Adapted from [102, 103]*

5.3.3.1 Secondary Electrons

Secondary electrons (SE) interact with the outermost surface of the material and are therefore very surface sensitive. They are generated from the electron shells of atoms as a consequence of being excited by the electrons in the electron beam (Figure 5.3b). The secondary electrons usually have an energy of less than 50 eV [102]; therefore, they can escape from the outermost region of the sample, as shown in Figure 5.3a. As a result, they provide the best resolution for imaging and provide more topological information than the back-scattered electrons [103].

5.3.3.2 Back-scattered Electrons

The back-scattered electrons (BSE) are highly energetic electrons that are produced when an electron from the electron beam is elastically scattered at the nucleus of an atom (Figure 5.3c). Because they are highly energetic, their interaction volume is much higher than the secondary electrons, as shown in Figure 5.3a. However, higher interaction volume results in reduced image resolution and topographic contrast. Nevertheless, they provide more information about the elements in the material. The higher the atomic number, the greater number of incoming electrons are back-scattered, resulting in a so-called Z-contrast. Heavier elements appear brighter because more back-scattered electrons reach the detector, allowing to identify the compositional differences [103].

5.3.3.3 Energy dispersive X-ray analysis

Energy dispersive X-ray (EDX) analysis is used to obtain accurate information about the composition of the material. When an electron from the primary electron beam ejects an electron from the inner shell of an atom, the void is filled by an electron from the outer shell with higher energy. The energy difference between the shells is emitted as an X-ray photon, as shown in (Figure 5.3d). The energy difference between the shells is the characteristic of the element. The emitted X-ray photons are measured with an X-ray spectrometer to identify the elements in the material. Quantitative element information

can be measured using the intensity of the X-ray photon of specific energy. Since the X-rays are produced within the entire interaction volume, as shown in Figure 5.3a, the spatial resolution for the EDX analysis in SEM is in the order of micrometres [102].

5.3.4 X-ray diffraction

X-ray diffraction (XRD) is a non-destructive technique that provides information about structures, phases, preferred crystal orientations (texture), and other structural parameters such as crystallinity and average grain size. X-rays are generated by a cathode ray tube and filtered to produce a monochromatic beam of X-rays, which are directed onto the sample. The X-rays are diffracted by the crystal lattice of the sample. The diffracted X-rays are detected using a detector. The diffracted X-rays which are in phase (constructive interference) can be observed at specific angles 2θ if the conditions satisfy Bragg's law [104] (see Figure 5.4) as shown in Equation 5.3

$$n\lambda = 2d_{hkl}sin\theta \tag{5.3}$$

Where n is an integer and λ is the wavelength of the X-ray beam, and θ is the incidence/diffracted angle. Because of the random orientation of the planes in the material, all possible diffraction directions of the lattice can be obtained by scanning the sample over a range of angles. Diffraction at different atomic planes produces a diffraction pattern that contains information about the atomic arrangement within the crystal and is analyzed using powder diffraction files.

Grazing incidence X-ray diffraction was used to analyze the crystal phases of the oxide scales formed during the exposure. The X-rays from the source are incident at a fixed angle (usually from 0.2°to 2°). A moving detector is used to detect X-rays at different angles. A Seimens D5000 diffractometer is used with Cu K_α radiation having a wavelength of 1.54 Å. The detector is scanned in the angular range of 20°- 70°.

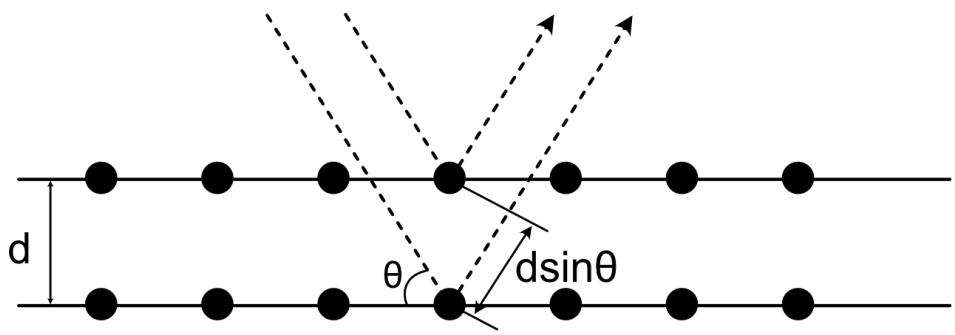

Figure 5.4: *Schematic representation of Bragg's law. Adapted from [104]*

5.3.5 Area Specific resistance

To ASR measurements were performed ex-situ on the exposed coupons. To achieve a good electrical connection with the oxide layer, an area of 10 mm x 10 mm was sputtered with platinum for 10 minutes using a Quorum 150 sputter coater and a sputter current of 60 mA. The sputtered area was further painted with platinum paste (Metalor 6926). The samples were exposed to a temperature of 150 °C for 15 minutes and 800 °C for 1 hour to remove all binders from the platinum paste and to sinter platinum paste (see Figure 5.5). The ASR was measured using a 4-point probe method in DC mode using platinum electrodes. An electrical current of 100 mA was used for the ASR measurements. The current was supplied using a Keithley 2400 source meter. To check the semiconducting behaviour, the ASR was measured as the coupon was cooled down. More details on the setup can be found in [105]

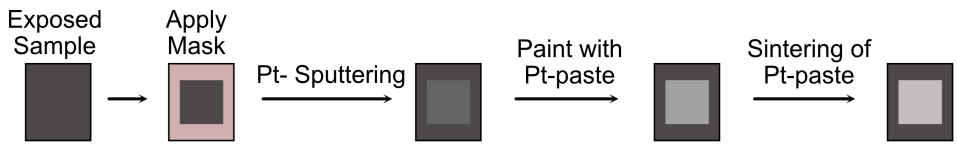

Figure 5.5: *Schematic illustration of the step wise electrode preperation process for ASR measurement.*

6 Results and Discussion

The chapter results and discussion is divided into two sections. The first part deals with the Balance of Plant (BOP) materials, and the second part investigates different steels and steel-coating combinations for interconnect applications.

6.1 BOP materials

Of the various metallic materials available for use in BOP components, four different groups of materials, chromia forming ferritic steel, alumina forming ferritic steel, Fe-base austenitic steel, Ni-base alloy, are examined for their potential application in the BOP. Table 5.1 (see section 5.1) lists 5 different alloys together with their composition. The performance of these alloys was evaluated in a typical air side environment for 500 hours at 650 and 850 °C. Additionally, to understand the effect of pre-oxidation, the coupons were pre-oxidized at 900 °C for 24 hours and were further exposed at 650 °C for 500 hours. The mass gain due to pre-oxidation is reported in Paper 1. The mass gain plots of the pre-oxidized alloys in the following sections represent oxidation kinectics after pre-oxidation, thus, did not include the mass gain due to pre-oxidation.

6.1.1 AISI 441 and AISI 444

Figure 6.1a shows that the chromium evaporation of 444 is slightly lower than that of 441 at 650 °C on the as-received coupons. The chromium evaporation of the pre-oxidized 441 and 444 is similar and about 30% lower than the as-received. At 850 °C, the chromium evaporation of as-received 444 and 441 is similar and higher than at 650 °C.

Both steels showed mass loss after 500 hours at 650 °C on as-received and pre-oxidized coupons (Figure 6.1b). The mass loss of 441 and 444 is similar in the respective exposure conditions. The net mass gain behaviour of the as-received coupons at 650 °C indicates paralinear oxidation kinetics. As discussed in the section 3.4, chromium evaporation significantly affects the oxidation behaviour. Because of the oxide lost through chromium evaporation, the gravimetrically measured mass gain (net mass gain) doesn't indicate the true extent of oxidation. Thus, the net mass gain should be compensated by the mass loss due to chromium evaporation to determine the true extent of oxidation, called corrected mass gain (see paper 1 for more details). The net and corrected mass gain of 441 and 444 at 650 °C are shown in Table 6.1. No major difference in the corrected mass gain of 444 and 441 is observed at 650 °C for as-received and pre-oxidized coupons. At 850 °C, a considerable difference is observed in the net and corrected mass gains of the as-received coupons. 441 showed a much higher net mass gain than that of 444 after 500 hours. Since the chromium evaporation is similar, the corrected mass gain of 441 is also higher than 444. Even after pre-oxidation for 24 hours at 900 °C, a significant difference in mass gain is observed between 441 and 444. This indicates that the oxidation kinetics of 444 is lower than 441 and agrees well with previously published data [79].

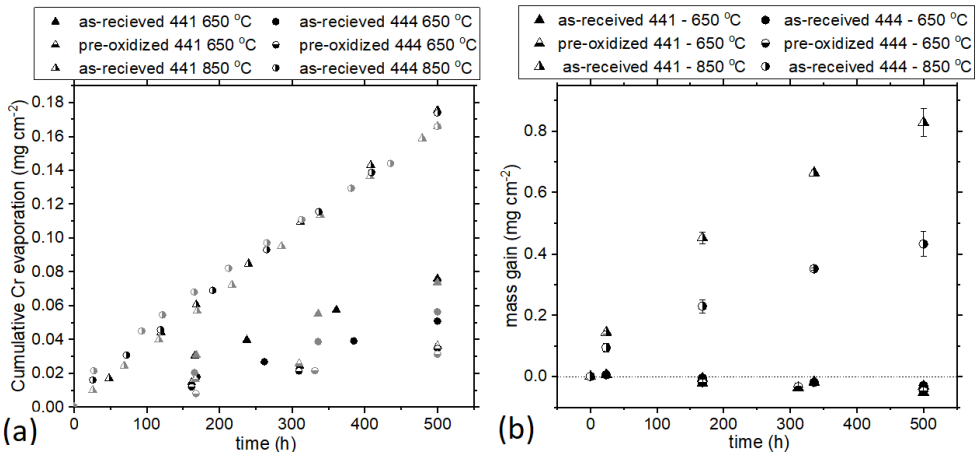

Figure 6.1: *(a) Chromium evaporation and (b) net mass gain as a function of time for the as-received and pre-oxidized 441, 444 exposed at 650 °C and as-received 441, 444 exposed at 850 °C for 500 h. Open and filled symbols represent two individual exposures.*

Table 6.1: Net mass gain and corrected mass gain in $mgcm^{-2}$of 441 and 444 exposed in as-received and pre-oxidized condition for 500 h at different temperatures

Material	**as-received (650 °C)**		**pre-oxidized (650 °C)**		**as-received (850 °C)**	
	net	**corrected**	**net**	**corrected**	**net**	**corrected**
441	-0,0307	0,0769	-0,051	0,0025	0.8275	1.0764
444	-0,0295	0,0526	-0,048	0,0015	0.4316	0.6417

The oxide scale thickness and structure of 441 and 444 after 500 hours on the as-received samples at 650 °C is similar. It is composed of a continuous Cr_2O_3 scale and discontinuous $(Cr, Mn)_3O_4$ spinel on the top (see paper 1). The oxide scale structure of 441 and 444 at 850 °C, revealed by EDX maps in Figure 6.2, is similar with an inner continuous Cr_2O_3 scale and continuous $(Cr, Mn)_3O_4$ spinel on the top. Such an oxide scale structure is expected for the pre-oxidized 441 and 444. The oxide scale of 441 and 444 at 850 °C (Figure 6.2) revealed a thinner oxide scale on 444 (2-3 μm) compared to 441 (3-4 μm). The thickness of the oxide scale matches well with the observed net mass gain (Figure 6.1b). Slower oxidation kinetics of 444 compared to 441 is suggested to be because of the higher volume fraction of laves phases in 444 [106].

The lower chromium evaporation of pre-oxidized coupons than the as-received coupons at 650 °C might be due to continuous $(Cr, Mn)_3O_4$ spinel on the surface of the pre-oxidized coupons. $(Cr, Mn)_3O_4$ is reported to decrease chromium evaporation by a factor of 2-3 times at 800 °C [25]. The chromium evaporation at 850 °C is 6 times higher than on the pre-oxidized coupons at 650 °C. These results agree with Falk-Windisch et al. [107] who has reported that chromium evaporation of similar alloys with similar oxide

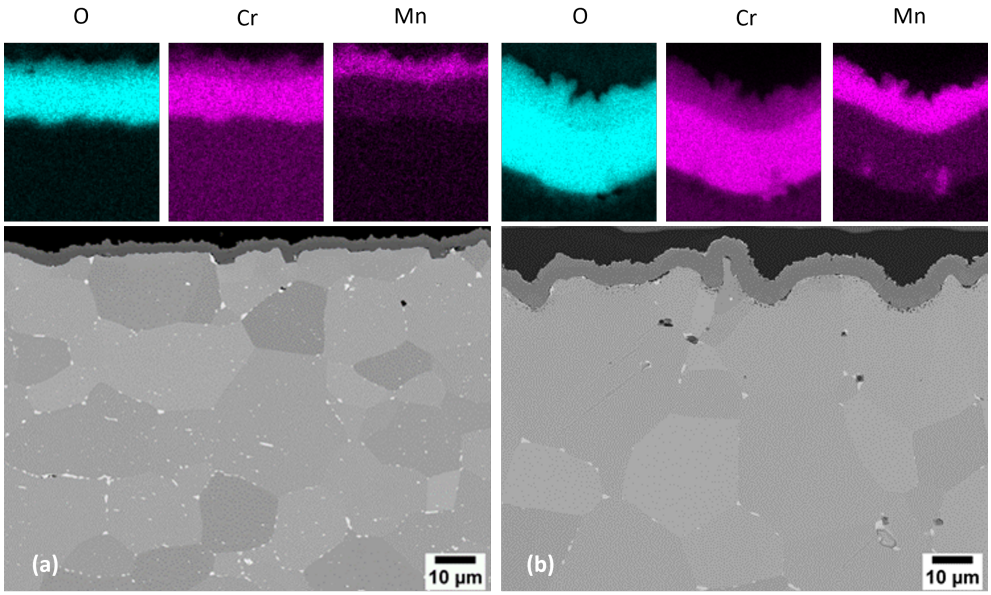

Figure 6.2: *SEM cross-section micrographs of (a) 444 and (b) 441 exposed at 850 °C for 500 h.*

scale increases by a factor of 2-3 per 100 °C in this temperature range. The pre-oxidized 441 and 444 showed a continuous mass loss due to slow oxidation kinetics, which can be attributed to the oxide scale formed during pre-oxidation. The corrected mass gain of the pre-oxidized coupons is lower than the as-received coupons as shown in table 6.1. This indicates an improvement in the oxidation behaviour after pre-oxidation.

6.1.2 Alloy 600

The chromium evaporation of chromia forming Ni-base material, alloy 600, shown in Figure 6.3a, is 2-3 times lower than that of 441 and 444 at the respective investigated temperatures. The chromium evaporation of the as-received coupons is 4 times lower at 650 °C than at 850 °C. The pre-oxidized coupons showed about 50% lower chromium evaporation than the as-received coupons at 650 °C. Furthermore, the pre-oxidized coupons showed a mass loss while the as-received coupons showed mass gain at 650 °C. Despite the change in the oxidation kinetics at 850 °C compared to 650 °C, the net mass gain is similar for as-received coupons (Figure 6.3b) at both temperatures after 500 hours.

The cross-section of alloy 600 at 650 °C after 500 hours, shown in Figure 6.4a, reveals a non-uniform oxide scale with thick nonprotective and thin protective regions. In the regions with a thick non-protective oxide scale, the oxide scale grew both inward (craters) and outward (islands) faster than the surrounding area. The surface morphology (inset in Figure 6.4a) shows that the islands are distributed over the entire surface, with varied

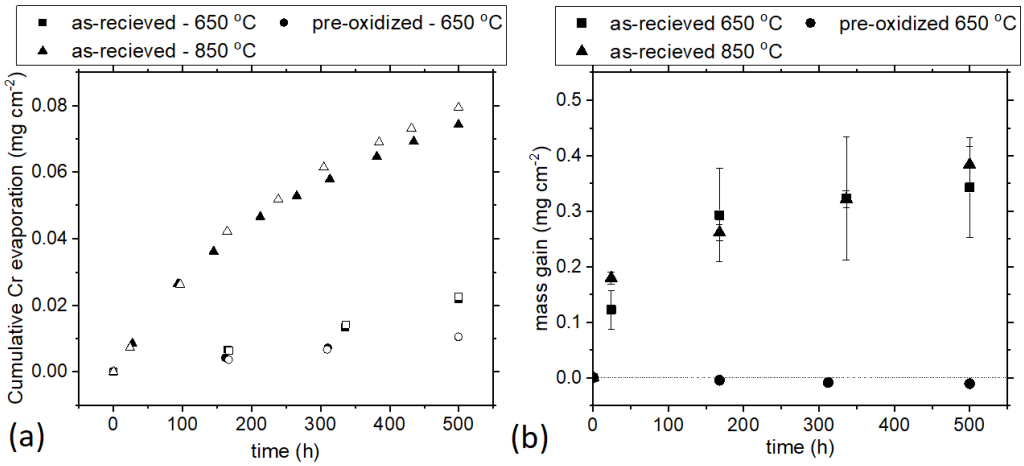

Figure 6.3: *(a) Chromium evaporation and (b) net mass gain as a function of time for the as-received and pre-oxidized alloy 600 exposed at 650 °C and as-received alloy 600 exposed at 850 °C for 500 h. Open and filled symbols represent two individual exposures.*

thickness in the range of 1 - 10 μm. EDX maps in Figure 6.4a revealed that the crater and the islands have varying local enrichments. The islands are rich in Ni and Fe oxides and are depleted in Cr. Oxidation proceeded inwards because of the lack of a protective layer resulting in a crater rich in Ni and Cr. XRD analysis showed the presence of NiO and $NiCr_2O_4$ in the oxide scale (see paper 1). Chromium enrichment is observed at the metal-oxide interface as the inward growing oxide scale is healed by forming a protective Cr rich scale.

The regions with a thin oxide scale could not be resolved in the SEM, and the lack of internal oxidation indicates the presence of a protective oxide scale. The protective scale was probably formed due to an enhanced chromium supply in this region. It may be related to the local microstructure of surface, such as grain orientation, high local dislocation density, and proximity to the high density of alloy grain boundaries. The lack of a continuous protective oxide scale resulted in higher net mass gain observed at 650 °C which is similar to the net mass gain at 850 °C.

The cross-section of alloy 600 at 850 °C after 500 hours, shown in Figure 6.4b, reveals a non-uniform oxide scale with varied thickness. The oxide scale is thicker above the alloy grains and thinner above the alloy grain boundaries. The EDX analysis in Figure 6.4b shows that the oxide scale above the alloy grains has a Ni-rich phase, NiO, on the top, followed by a Fe and Ni-rich intermediate oxide scale featuring local enrichment and chromia scale at the metal-oxide interface. The intermediate Fe and Ni-rich oxide layer is absent on the top of alloy grain boundaries, resulting in a thinner scale. This difference in the oxide scale structure arises due to the higher Cr diffusion along the alloy grain

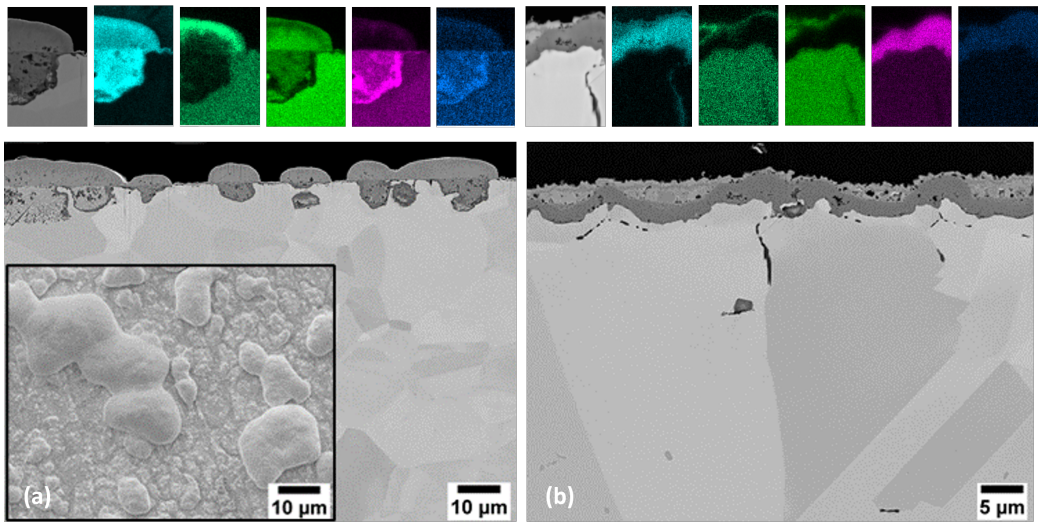

Figure 6.4: *SEM cross-section micrographs and EDX maps of alloy 600 exposed at (a) 650 °C and (b) 850 °C for 500 h.*

boundaries than the bulk in Ni-base alloys [108]. Moreover, the alloy grain boundaries also act as preferential nucleation sites for the Cr-rich oxide scale [109]. This resulted in faster formation of chromia scale on the grain boundaries than surrounding area. The formation of the Ni-rich cap layer resulted in lower chromium evaporation compared to ferritic stainless steels, 441 and 444 at the investigated temperatures.

Upon pre-oxidation, the performance of alloy 600 is improved at 650 °C. The pre-oxidized coupons have a similar oxide scale structure to those exposed at 850 °C. The low corrected mass gain on the pre-oxidized coupons is due to the presence of a continuous protective chromium-rich oxide scale. The chromium evaporation is lower on the pre-oxidized coupons because of the thick Ni-rich cap layer formed upon pre-oxidation.

6.1.3 Alloy 800H

The chromium evaporation of chromia forming austenitic steel, alloy 800H, shown in Figure 6.5a, is 5 - 10 times lower than that of 444 and 441 at the respective investigated temperatures. The chromium evaporation at 650 °C is 10 times lower than at 850 °C. The pre-oxidized coupons showed similar chromium evaporation as the as-received at 650 °C. Alloy 800H had the highest Cr content among the selected alloys; however, it exhibited the highest mass gain (Figure 6.5b) at both investigated temperatures on the as-received coupons. Nevertheless, the mass gain of the pre-oxidized coupons is extremely low. Table 6.2 shows that as-received alloy 8000H exhibited inverse temperature behaviour where lower mass gains are observed at higher temperatures. The mass gain at 650 °C is 4-5 times higher than at 850 °C after 500 hours. The higher mass gain indicates the

low oxidation resistance at 650 °C. However, the mass gain stabilized after 168 hours, revealing a decrease in oxidation rate with time.

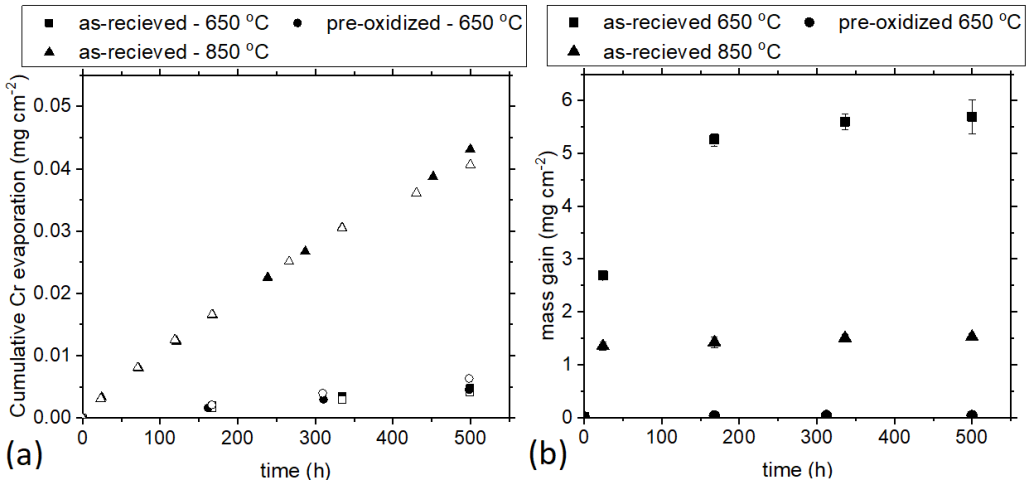

Figure 6.5: *(a) Chromium evaporation and (b) net mass gain as a function of time for as-received and pre-oxidized alloy 800H exposed at 650 °C and as-received alloy 800H exposed at 850 °C for 500 h. Open and filled symbols represent two individual exposures.*

Table 6.2: Mass gain of alloy 800H exposed at different temperatures for 24 h.

Temperature	**650 °C**	**850 °C**	**900 °C**
Mass Gain ($mg\ cm^{-2}$)	2.82	1.35	0.71

The cross-section of alloy 800H at 650 °C after 500 hours, shown in Figure 6.6a reveals that the oxide scale is continuous and nonuniform with the thickness varying from 15 to 70 μm. The oxide scale has outward and inward growing parts, and the labels 1,2, and 3 show three distinct oxide scales. The outer scale (layer 1) is rich in Fe, and the scale beneath (layer 2) is rich in Fe and Ni. Between layers 2 and 3, discontinuous patches of Ni-rich oxide (EDX map of Ni in Figure 6.6a) are observed at the original interface of the alloy. Layer 3 is an inward growing intermediate oxide layer rich in Cr, Mn, Ni, and Fe. The concentration of Cr in the oxide is highest at the metal-oxide interface. Despite the higher diffusion coefficient (D) of Cr among Fe, Cr, and Ni in Fe-Cr-Ni austenitic steels [110], the protective chromia scale is not formed on alloy 800H at 650 °C during the initial stage. This led to the formation of fast-growing oxides, resulting in high mass gain observed during the initial period. In this stage, Fe and Cr preferentially oxidized to form fast-growing iron-rich $(Fe, Cr)_2O_3$ on the surface by outward diffusion due to higher miscibility and diffusion coefficient. Simultaneously, inward diffusion of dissolved oxygen oxidized Ni to NiO. The oxidation proceeded inwards, oxidizing Fe, Cr, and Ni due to the lack of a protective scale.

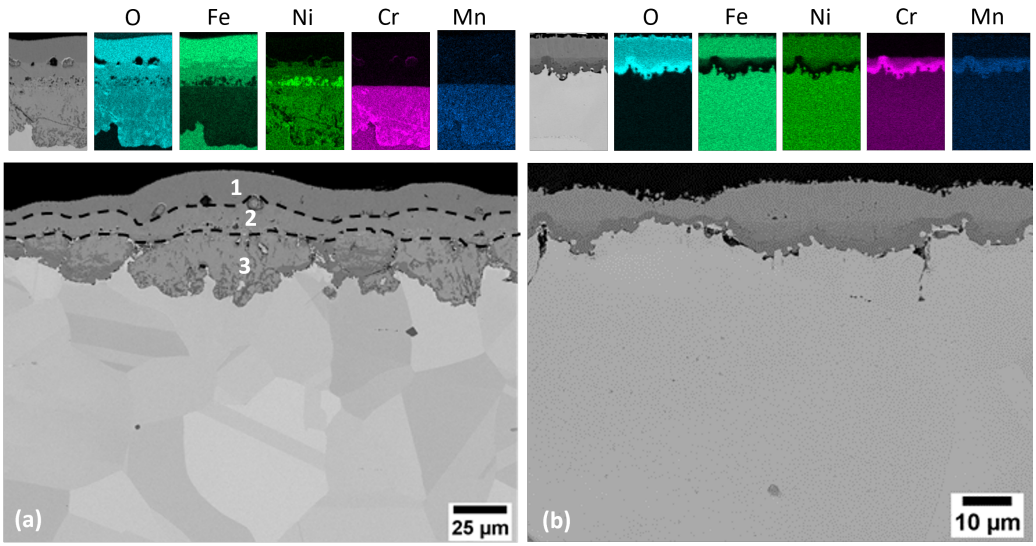

Figure 6.6: *SEM cross-section micrographs and EDX maps of alloy 800H exposed at (a) 650 °C and (b) 850 °C for 500 h.*

The oxide layer healed by forming a protective Cr rich oxide layer, inhibiting further rapid inward oxidation. The formation of the protective layer resulted in lower oxidation as observed in the mass gain after 168 hours in Figure 6.5b. The low chromium evaporation observed at 650 °C is due to the thick oxide scale, which limited Cr oxide access to the environment.

The oxide scale structure (Figure 6.6b) at 850 °C is similar to the one at 650 °C. However, at 850 °C, the oxide scale is thinner due to faster formation of a protective chromia scale at higher temperatures. The oxide scale structure and thickness is different above the alloy grains and alloy grain boundaries. Despite having 20% Cr in the steel, the Cr-rich scale is not formed on the surface like in 441 and 444 at 850 °C during the initial oxidation, instead formed a $(Fe, Ni)_3O_4$ spinel on the surface. This might be due to slower Cr diffusion in austenitic steels compared to the ferritic steels [111]. The oxidation proceeded further, resulting in the intermediate oxide layer rich in Cr, Mn, Fe and Ni, observed only above the alloy grains. Such scale is not observed above the alloy grain boundaries because the protective chromia scale formed much faster as the chromium diffusion along the grain boundaries is faster than the bulk [112]. As a result, a thinner oxide scale is observed above the alloy grain boundaries. Once a continuous protective Cr scale is formed at the metal-oxide interface, the oxidation rate slowed down, as reflected in the mass gain after 24 hours. The presence of the $(Fe, Ni)_3O_4$ spinel cap layer on the Cr rich oxide resulted in lower chromium evaporation observed in Figure 6.5a. Due to difference in the oxide scale structure of alloy 800H compared to 441 and 444, chromium evaporation increased by 10 times upon increasing the temperature from 650 °C to 850

°C.

The oxide scale formed upon pre-oxidation resembles the structure of the oxide scale at 850 °C; however, the outer spinel layer is thinner as the protective scale formed faster at higher temperatures. Despite the thinner cap layer on pre-oxidized coupons compared to as-received coupons, the chromium evaporation is similar at 650 °C. This indicates the effectiveness of the $(Fe, Ni)_3O_4$ spinel cap layer in reducing chromium evaporation. The protective oxide scale formed during pre-oxidation resulted in a lower mass gain during subsequent exposure at 650 °C.

6.1.4 A197/Kanthal® EF101

The chromium evaporation of alumina forming FSS, A197, shown in Figure 6.7a, is two orders of magnitude lower than that of 441 and 444, the lowest of the selected alloys at both temperatures. The results are in agreement with previous studies on the chromium evaporation of alumina scale forming alloys [25]. The chromium evaporation at 650 °C is 4 times lower than the chromium evaporation at 850 °C. The chromium evaporation is similar for as-received coupons and pre-oxidized coupons. The mass gain of A197, shown in Figure 6.7b, is extremely low at the investigated temperatures. A197 has the lowest corrected mass gain of the selected alloys at both temperatures, indicating superior oxidation resistance.

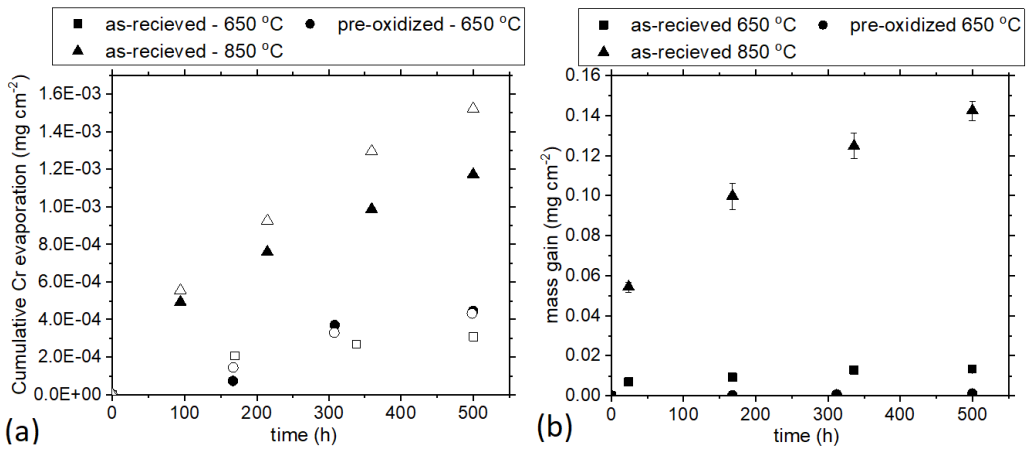

Figure 6.7: *(a) Chromium evaporation and (b) net mass gain as a function of time for as-received and pre-oxidized A197 exposed at 650 °C and as-received A197 exposed at 850 °C for 500 h. Open and filled symbols represent two individual exposures.*

The cross-section of A197 at 650 °C after 500 hours, shown in Figure 6.8a, reveals the presence of a continuous protective oxide scale. The oxide scale has a thickness of 50 nm

after 500 hours. The oxide scale is too thin for EDX analysis in SEM. However, based on the chromium evaporation and mass gain data, it can be assumed that the oxide scale is an alumina rich scale. The cross-section of A197 at 850 °C after 500 hours, shown in Figure 6.8b, reveals a multi-layered oxide with dense inner and porous outer scales. The oxide scale is mostly uniform, with a thickness of about 500 nm after 500 hours. Reactive element oxides are sporadically observed in the oxide scale, and the oxide scale is thicker in those regions. EDX maps in Figure 6.9 showed the presence of an alumina rich oxide. Sand et al [113] has confirmed the presence of mullite ($Al_x(Al_{2+2x}Si_{2+2x})O_{10-x}$) and tridymite ($SiO_2$ polymorph) in addition to α and γ alumina when A197 was exposed at 800 °C in 20% H_2O.

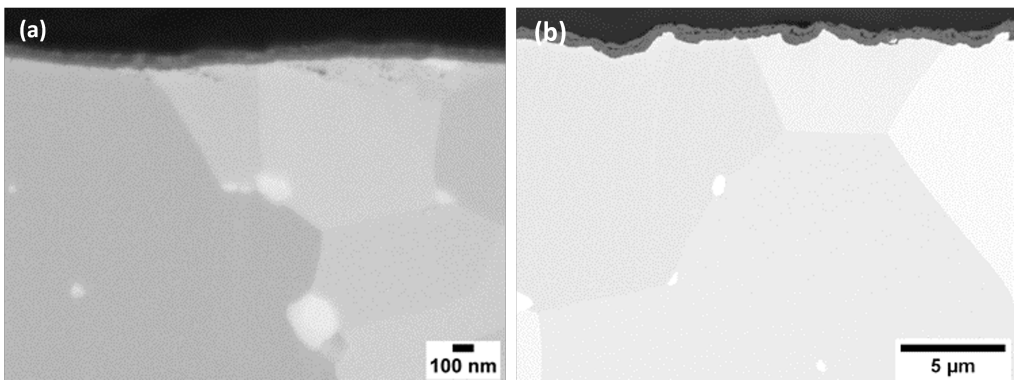

Figure 6.8: *SEM cross-section micrographs of A197 exposed at (a) 650 °C and (b) 850 °C for 500 h.*

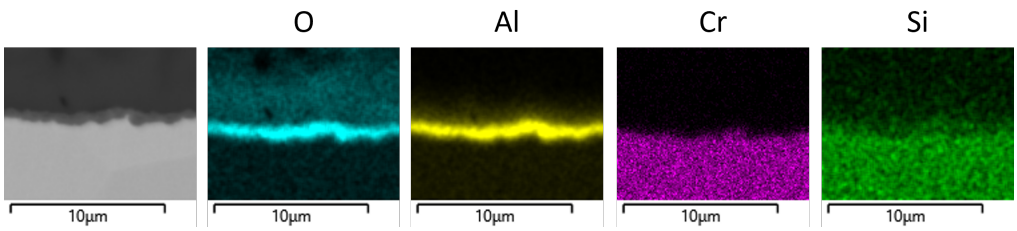

Figure 6.9: *EDX maps of the cross-section of A197 exposed at 850 °C for 500 h.*

The pre-oxidized A197 showed almost no change in mass when further exposed at 650 °C for 500 hours. This is due to the alumina scale formed up on pre-oxidation. Table 6.3 shows that the mass gain of as-received after 24 hours is 10 times lower than the mass gain due to pre-oxidiation for 24 hours. Nevertheless, chromium evaporation of the as-received and pre-oxidized coupons is similar (Figure 6.7a). This indicates that the oxide scale formed at 650 °C is extremely effective in reducing the chromium evaporation, similar to the α and γ alumina scale. Extremely low chromium evaporation and mass

gain make A197 particularly suitable for BOP application.

Table 6.3: Mass gain of A197 exposed at different temperatures for 24 h.

Temperature	**650 °C**	**900 °C**
Mass Gain ($mg\ cm^{-2}$)	0.007	0.078

6.1.5 Comparison of the selected steels

Of the as-received alloys exposed at 650 °C, 441 and 444 exhibited the highest chromium evaporation and mass loss after 500 hours. Alloy 600 showed about 3 times lower chromium evaporation than 441 and 444. Alloy 800H showed 10 times lower chromium evaporation than 441 and 444. However, the mass gain of alloy 800H is very high, indicating inferior oxidation resistance. Alloy 600 and alloy 800H formed a cap layer on a Cr-rich scale due to inferior oxidation resistance. However, this cap layer helped to reduce chromium evaporation. A197 showed about 100 times lower chromium evaporation than 441 and 444. The mass gain of A197 is the lowest of the selected alloys, indicating superior oxidation resistance. Except for A197, all the alloys showed poor behaviour either in terms of chromium evaporation or oxidation resistance.

In general, the chromium evaporation of the selected alloys is higher at 850 °C than at 650 °C. Nevertheless, the ranking of the alloys according to chromium evaporation is similar to 650 °C. All alloys showed net mass gain, alloy 800H had the highest and A197 had the lowest net mass gain. A Ni-rich cap layer is formed on the top of the protective chromia layer on alloy 800H and alloy 600. Due to the inferior cap layer on alloy 600, the chromium evaporation is higher than alloy 800H. A197 formed an alumina scale and therefore has the lower chromium evaporation and mass gain.

Pre-oxidation significantly improved the performance of the alloys at 650 °C. The chromium evaporation of the pre-oxidized alloys is 30 - 50 % lower than the as-received except for A197 and alloy 800H, which showed similar chromium evaporation under both conditions. The ranking of the materials in terms of chromium evaporation is similar to the as-received. Pre-oxidation resulted in a significant improvement in the oxidation resistance of alloy 600 and alloy 800H. Cost is an important factor in the material selection for BOP components. Alloy 600 is expected to be the most expensive, followed by alloy 800H and ferritic steels A197, 441 and 444. Of the ferritic steels, A197 is expected to be expensive due to lower production volumes than 441 and 444.

6.2 Interconnects

The major challenges for the widespread commercialization of solid oxide fuel cell technology are long-term system stability and material costs. The choice of the steel-coating combination for the interconnect strongly affects the challenges as mentioned above. Since the interconnect is a significant part of the total stack cost [2, 3], using ferritic steels such as 441 and 444 results in a lower cost than tailor-made steels such as Crofer 22 APU. However, it is crucial to understand the behaviour of low-cost steels and compare them to tailor-made steel. The behaviour of the uncoated steels and coated steels is compared up to 1000 hours at 800 °C in the simulated air side of SOFC.

6.2.1 Uncoated steels - Chromium evaporation and Gravimetric measurements

The cumulative chromium evaporation of the uncoated steels, shown in Figure 6.10a, is dissimilar. 444 showed the highest cumulative chromium evaporation followed by 441 and Crofer 22 APU. Figure 6.10b shows that the rate of chromium evaporation decreases with time on all the steels, followed by a steady-state rate. This is because of Mn diffusion into the oxide scale forming $(Cr, Mn)_3O_4$ spinel, which reduces the chromium evaporation by a factor of 2-3 compared to the Cr_2O_3 scale [25, 38]. 444 showed a high rate of chromium evaporation initially and took longer to reach the steady-state chromium evaporation compared to 441 and Crofer 22 APU, thus resulting in the highest cumulative Cr evaporation. It is speculated that slow Mn diffusion to the oxide scale resulted in such behaviour (see paper 3). Nevertheless, after 500 hours, the rate of chromium evaporation is similar on 441, 444 and slightly lower on Crofer 22 APU.

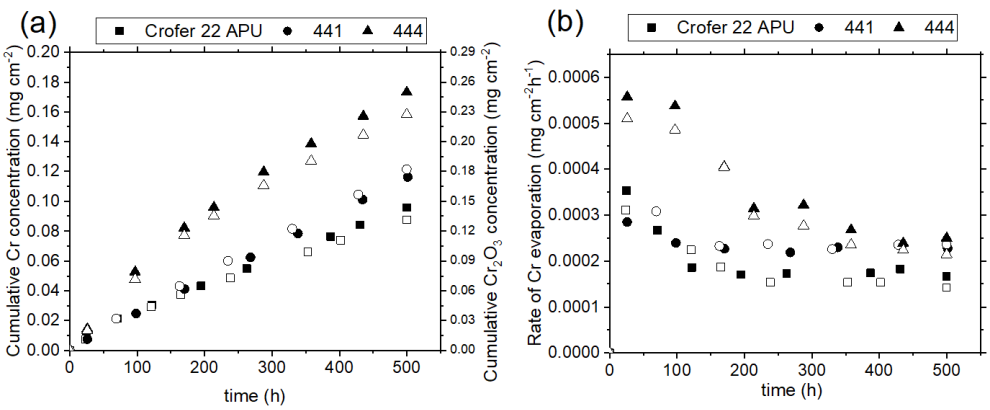

Figure 6.10: *(a) Cumulative chromium evaporation (b) rate of chromium evaporation as a function of time for the uncoated Crofer 22 APU, 441 and 444 exposed at 800 °C for 500 h continuously. Open and filled symbols represent two individual exposures.*

The net mass gains of the selected uncoated steels, shown in Figure 6.11a, differ significantly after 500 hours. 441 has the highest net mass gain, followed by Crofer 22 APU, and 444. 441 and Crofer 22 APU showed a continuous increase in net mass with time, while 444 had a rapid mass gain initially followed by a slow mass gain for the rest of the exposure. As discussed in Section 6.1.1, the net mass gain is influenced by chromium evaporation. Corrected mass gain, shown in Figure 6.11b, is higher than the respective net mass gain of the steels, indicate the true extent of oxidation. Due to high chromium evaporation of 444, the corrected mass gain is similar to Crofer 22 APU, and 441 has the highest corrected mass gain.

The differences observed in the oxidation behaviour of the uncoated steels is probably due to the influence of different alloying elements in the steel. A significant difference is observed between the corrected mass gain of 441 and Crofer 22 APU. This might be due to the presence of a reactive element, La, in Crofer 22 APU, which is known to significantly improve the high temperature oxidation behaviour as discussed in section 4.1.1.1. Despite the lack of reactive elements, 444 had a much lower corrected mass gain than 441. Similar trend is also observed at 850 °C as shown in the section 6.1.1.

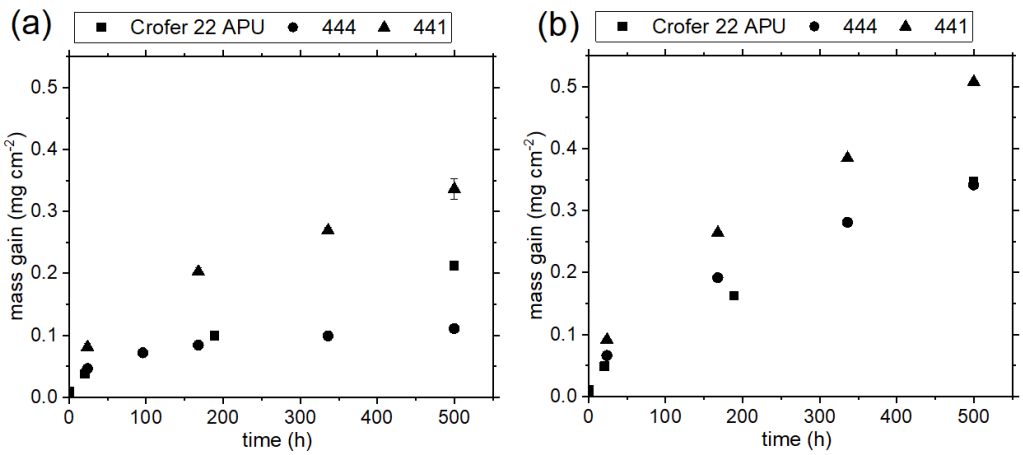

Figure 6.11: *(a) Net mass gain and (b) Corrected mass gain of uncoated steels exposed at 800 °C for 500 hours.*

6.2.2 Uncoated steels - Microstructural Evolution

The SEM micrographs and EDX maps of the cross-sections of the uncoated steels after 500 hours, shown in Figure 6.12, reveal that the thickness of the oxide scale differed in the uncoated steels. 444 has the thinnest oxide scale followed by Crofer 22 APU and 441. The observed oxide thicknesses matches well with the net mass gains in Figure 6.11a. Ti internal oxidation is observed under the metal-oxide interface of 441 and Crofer 22 APU. Laves phase precipitates are observed in the steel matrix in 441 and 444. The oxide scale structure of all uncoated steels is similar, composed of an outer $(Cr, Mn)_3O_4$ spinel and inner Cr_2O_3 scale, after 500 hours. The presence of outer $(Cr, Mn)_3O_4$ spinel on all the steels resulted in a similar rate of chromium evaporation.

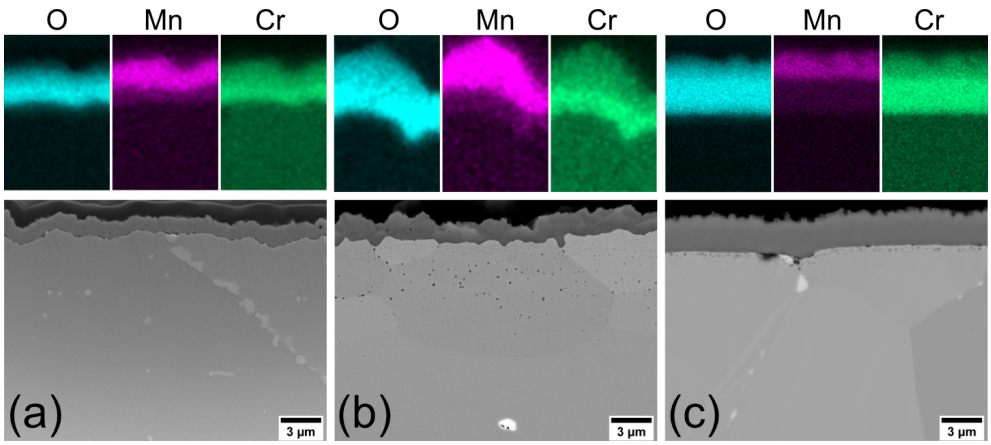

Figure 6.12: *SEM cross-section micrographs and EDX maps of (a) 441 (b) Crofer 22 APU (c) 441 exposed at 800 °C for 500h.*

6.2.3 Coated steels - Chromium evaporation

The cumulative chromium evaporation of Ce/Co coated steels performed on coupons cut from steel sheet (sheet-coated coupons), shown in Figure 6.13, follows a similar trend as the uncoated steels. However, the chromium evaporation after 500 hours is 10 times lower compared to the uncoated. These results are consistent with earlier published data on Ce/Co coatings [56, 69, 82, 81, 114, 115]. Since the sheet-coated coupons have uncoated edges, the chromium evaporation measured has a contribution from the uncoated edges. The uncoated edges contribute to 3.6 % of the total area. The chromium evaporation of the uncoated 444 is highest of the selected steels. On the sheet coated coupons, chromium evaporated from the uncoated edges of sheet-coated 444 is higher than sheet-coated 441 and Crofer 22 APU. Thus, the data in Figure 6.13 does not represent the actual effect of Ce/Co coatings in inhibiting chromium evaporation. To understand the true effect of Ce/Co coatings in reducing chromium evaporation, coupons coated entirely with the Ce/Co coating are evaluated.

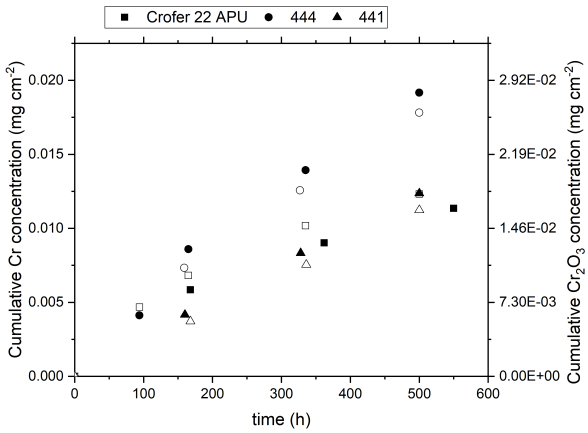

Figure 6.13: *Cumulative chromium evaporation as a function of time for the Ce/Co sheet-coated steels exposed at 800 °C for 500 h continuously. Open and filled symbols represent two individual exposures.*

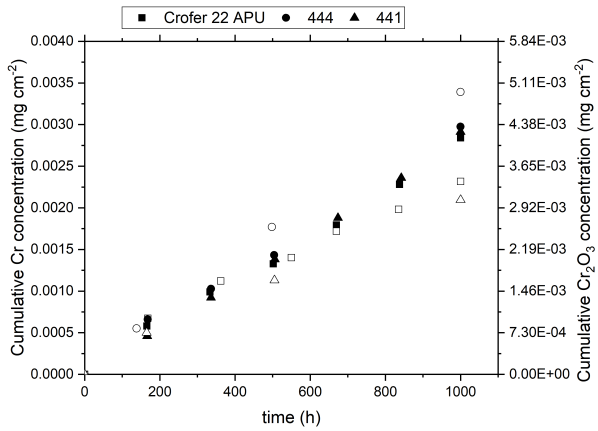

Figure 6.14: *Cumulative chromium evaporation as a function of time for the Ce/Co precut-coated steels exposed at 800 °C for 1000 h continuously. Open and filled symbols represent two individual exposures.*

Despite PVD being a line-of-sight process, some coating material is deposited on the edges of the precut-coated coupons. Thus, these coupons have coated faces and coated edges. Figure 6.14 shows that the cumulative chromium evaporation of all the precut-coated steels is similar, unlike the uncoated and sheet coated. Moreover, the chromium evaporation of the pre-cut coupons is significantly lower than the sheet-coated coupons. The rate of chromium evaporation is extremely low and did not change much throughout

the exposure (see paper 3). The cumulative chromium evaporation of pre-cut coated steels is at least 60 times lower than the uncoated coupons after 500 hours. Due to the high chromium evaporation of uncoated 444, the chromium evaporation of the coated 444 is almost 100 times lower than the uncoated. Based on the data from sheet-coated coupons and precut-coated coupons, it can be observed that uncoated edges significantly influence the chromium evaporation measurements.

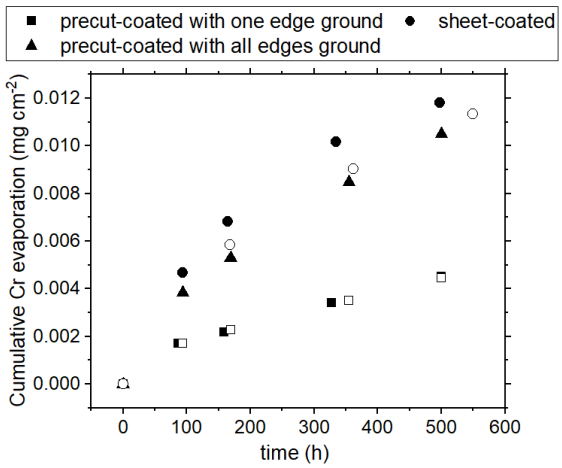

Figure 6.15: *Cumulative chromium evaporation as a function of time for the Ce/Co precut-coated with one ground edge, precut-coated with all ground edges and sheet-coated exposed at 800 °C for 500 h continuously. Open and filled symbols represent two individual exposures.*

To further confirm this hypothesis, one edge and all edges of precut-coated Crofer 22 APU were ground to #1200 to remove the coating from the edges, called precut-coated with one ground edge and precut-coated with all ground edges, respectively. Figure 6.15 shows that the cumulative chromium evaporation of sheet-coated and precut-coated with all ground edges is similar. The precut-coated with one ground edge has lower chromium evaporation than the precut-coated with all ground edges. Moreover, the precut-coated with one ground edge has 3 times higher chromium evaporation than the precut-coated coupons. The rate of chromium evaporation decreased with time on the precut-coated with either one or all ground edges (see paper 2).

Based on the chromium evaporation data from Figure 6.10a and Figure 6.14a, the chromium evaporation for sheet-coated coupons (similar to precut-coated with all ground edges), precut-coated with one ground edge is calculated and compared to the experimental observations. The uncoated and coated areas are calculated and multiplied with the corresponding cumulative chromium evaporation per unit area for 500 hours, assuming that the uncoated edges have the same evaporation rate per unit area as the uncoated steels. Table 6.4 shows that there is a significant difference in the calculated and measured

chromium evaporation of the precut-coated coupons with ground edges. This clearly indicates that the uncoated edges contributed to higher chromium evaporation than the corresponding area. It is speculated that the flow dynamics inside the reactor resulted in higher chromium evaporation from the edges.

Table 6.4: Experimental and calculated cumulative chromium evaporation of sheet-coated Crofer 22 APU and precut-coated Crofer 22 APU with one ground edge for 500 h.

	%Uncoated area	%Coated area	Calculated Cr evaporation ($mg\ cm^{-2}$)	Experimental Cr evaporation($mg\ cm^{-2}$)
sheet-coated	96.37	3.62	0.0046	0.011
precut-coated with one ground edge	99.15	0.85	0.0021	0.0045

6.2.4 Coated steels - Gravimetric measurements

6.2.4.1 Influence of substrate

The mass gain of the Ce/Co coated steels, shown in Figure 6.16, reveals that all the coated steels have similar mass gains after 1000 hours. During the first two hours, a rapid increase in the mass gain is observed due to the oxidation of the metallic Ce/Co coating. After that, all the steels showed a similar and continuous increase in mass following parabolic oxidation kinetics. Since the chromium evaporation is extremely low, the net mass gain and the corrected mass gain are similar for the coated steels. Similar mass gain on coated steels is remarkable considering the variation in behaviour of the uncoated steels. 444 showed slower oxide scale growth than 441 when uncoated at 850 °C (see section 6.1.1) and 800 °C (see section 6.2.1). But such differences are not observed when the steels are coated with Ce/Co.

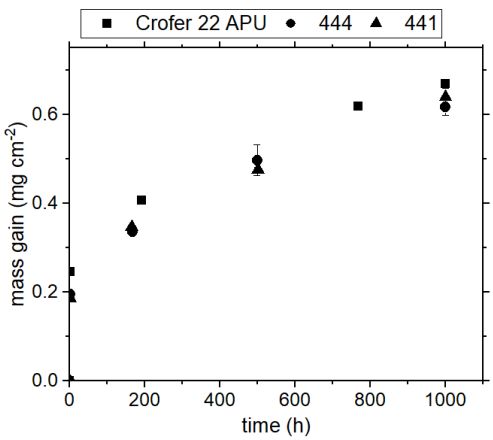

Figure 6.16: *Net mass gain of Ce/Co coated 441, 444, and Crofer 22 APU exposed at 800 °C for 1000 h.*

Earlier studies showed that the reactive elements greatly influence the oxidation kinetics of the chromia scale. Canovic et al.[74] has showed a significant decrease in the oxidation upon the addition of 10 nm Ce to 600 nm Co coating. It is speculated that the reactive elements in the coating caused this behaviour. Since the oxide scales formed on the coated steels have similar Ce doping, it resulted in similar oxidation behaviour. 441, which showed the highest mass gain when uncoated, has similar mass gain to others when coated. Thus, it can be concluded that the Ce/Co coating is particularly effective on 441.

6.2.4.2 Influence of Ce layer thickness

If 10 nm of Ce can have such a huge impact on the oxidation behaviour, it looks plausible that higher doping of RE might result in improved oxidation behaviour for the selected steels. As the oxide scale grows thicker, the doping per unit volume decreases, which might also affect the oxidation behaviour in the long term. To further enhance the effect of reactive elements, coatings with a thicker Ce layer are deposited on 441 as shown in Table 5.4. On the contrary to the expectation, the mass gain of 441 coated with different Ce thickness in Ce/Co coating, as shown in Figure 6.17, exhibited no difference till 6000 hours. It might be because the doping of the oxide scale with 10 nm of Ce in the coating is already enough to have the benefits of the reactive element effect.

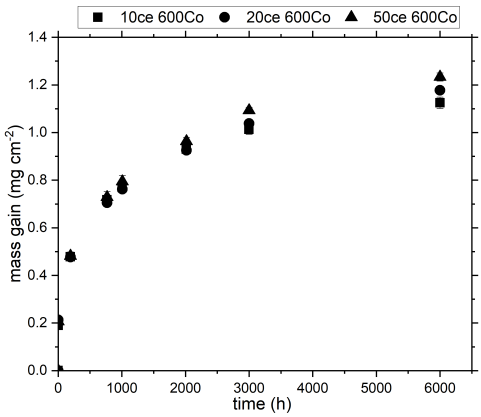

Figure 6.17: *Net mass gain of 10Ce600Co, 20Ce600Co, and 50Ce600Co coated 441 exposed at 800 °C for 6000 h.*

6.2.5 Coated steels - Microstructural Evolution

The SEM micrographs of the cross-sections of the Ce/Co coated steels, shown in Figure 6.18, exhibits the presence of two distinct layers in the oxide scale on all steels. From the EDX map in Figure 6.19, it can be concluded that the outer layer is $(Co, Mn)_3O_4$ spinel and the inner layer is Cr_2O_3. The presence of $(Co, Mn)_3O_4$ spinel on the chromia scale resulted in low chromium evaporation as observed in Figure 6.14 compared to the

uncoated steels which had outer $(Cr, Mn)_3O_4$ spinel. The chromia scale has a similar thickness on all coated steels, which matches well with the mass gains observed in Figure 6.16. A major difference between the steels is observed in the silicon map. 441 and 444 showed the formation SiO_2 subscale at the metal-oxide interface. Due to low Si content in Crofer 22 APU, no SiO_2 subscale is observed at the metal-oxide interface. Despite a higher fraction of laves phase in 444 than 441, SiO_2 subscale looks more prominent in 444 than 441. The reason for this is still unclear.

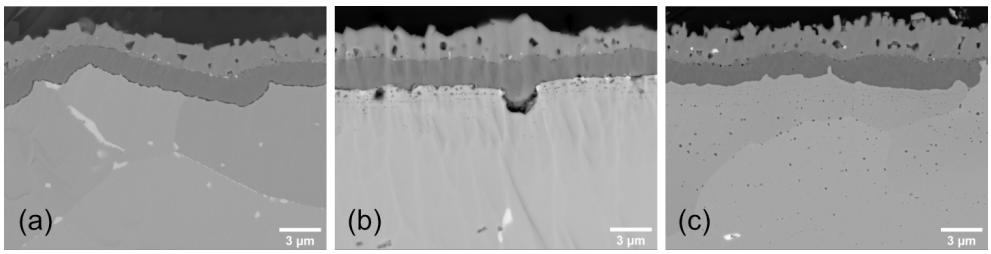

Figure 6.18: *SEM cross-section micrographs Ce/Co coated (a) 444 (b) 441 and (c) Crofer 22 APU exposed at 800 °C for 1000 h.*

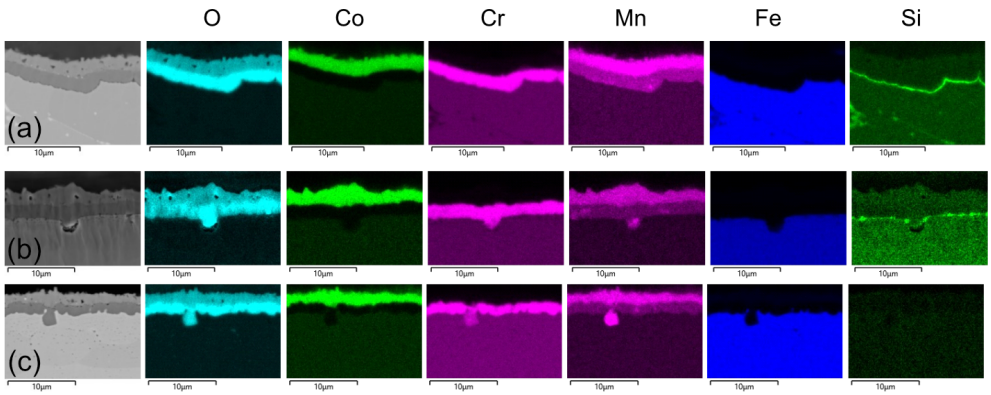

Figure 6.19: *EDX maps of the cross-section of Ce/Co coated (a) 444 (b) 441 and (c) Crofer 22 APU exposed at 800 °C for 1000 h.*

6.2.6 Coated steels - Area specific resistance

The Ce/Co coated steels performed better than the uncoated steels in chromium evaporation and oxide scale growth. So, Ce/Co coated steels are selected for the subsequent electrical characterization. Figure 6.20 shows that the ASR values of all coated steels are similar. This is surprising considering the Si scale observed in EDX maps of 444 and 441 after 1000 hours at the metal-oxide interface. SiO_2 has very high resistance, in the range of 10^{-5} to 10^{-7} Scm^{-1} [116] and is reported to be detrimental to conductivity of the interconnects [16]. However, the influence of the SiO_2 subscale is not observed

experimentally. It is speculated that the SiO_2 scale is not continuous or doped, which improved its conductivity. For the contribution of different oxides to the ASR, see paper 3.

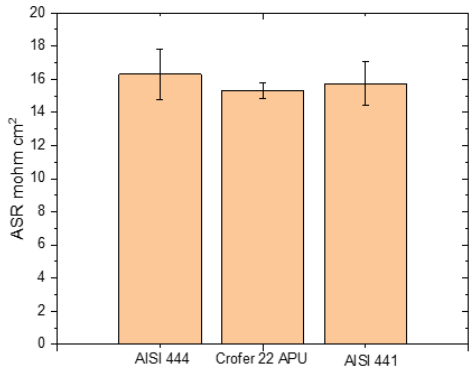

Figure 6.20: *ASR of the Ce/Co coated steels exposed at 800 °C for 1000 h. Error bars indicate standard deviation.*

7 Summary and Outlook

The findings in this thesis address the common degradation issues, chromium evaporation and oxide scale growth associated with the use of metallic materials in SOFC applications, whether as interconnects or construction materials for balance of plant components. All the exposures are conducted in a simulated air-side atmosphere of the SOFC. The main findings and important conclusions are listed below.

Balance of plant

Materials from four different groups were investigated at 650 °C and 850 °C, and their behaviour is related to the corresponding microstructure.

A197: The alumina forming alloy, A197, showed the formation of a slow-growing protective scale with excellent chromium retention properties at 650 °C. At 850 °C, it formed an alumina scale. It exhibited the lowest chromium evaporation of the selected alloys; two orders of magnitude lower than 441 and 444 at the investigated temperatures. The high oxidation resistance and low chromium evaporation make A197 a highly recommended material for BOP components.

Alloy 800H: The chromia forming Fe-base austenitic steel, alloy 800H, showed lower chromium evaporation than the selected alloys under all the exposure conditions, except A197. This was due to the formation of a cap layer on top of the Cr-rich scale, reducing Cr access to the environment. The oxide scale was composed of NiO and Fe_2O_3 oxides at 650 °C and $(Fe, Ni)_3O_4$ spinel at 850 °C. Low chromium evaporation makes alloy 800H interesting for BOP components. By contrast, oxidation behaviour at 650 °C was poor due to the lack of protective scale. However, an additional pre-oxidation step resulted in improved oxidation performance at 650 °C.

Alloy 600: The chromia forming Ni-base material, alloy 600, showed an intermediate performance among the selected alloys. It formed a cap layer of NiO on Cr-rich scale. Thus, the chromium evaporation was lower than 441 and 444, at all the investigated temperatures. However, alloy 600 showed poor oxidation behaviour at 650 °C. Considering the high cost of Ni-base materials, alloy 600 seemed poorly suited for BOP components.

441 & 444: The chromia forming ferritic steels, 441 and 444, showed similar chromium evaporation at both temperatures and at higher levels than those of the other selected alloys. After 500 hours, the oxide scale comprised an outer $(Cr, Mn)_3O_4$ and inner Cr_2O_3 scale. High chromium evaporation and oxide-scale growth made them particularly unsuitable for BOP components.

During operation, some of the BOP components might also experience fuel and dual atmosphere (fuel and air on either side) conditions. Future research should focus on the

oxidation behaviour and chromium evaporation characteristics of these alloys in fuel and dual atmosphere conditions. Other aspects relevant for the material selection of BOP components, such as strength, long-term creep, and weldability, must be explored.

Interconnects

The low-cost steels, 441 and 444, were benchmarked against Crofer 22 APU in uncoated and coated conditions for the interconnect application at 800 °C.

Uncoated steels showed differences in chromium evaporation and oxidation behaviour. 444 had the highest chromium evaporation, followed by 441 and Crofer 22 APU. However, after 500 hours, the rate of chromium evaporation was similar for 441 and 444 but slightly lower for Crofer 22 APU. 441 had the highest net mass gain, followed by Crofer 22 APU and 444. The corrected mass gains were similar for Crofer 22 APU and 444, due to the higher chromium evaporation of 444. After 500 hours, the oxide scale structure of the uncoated steels was similar with outer $(Cr, Mn)_3O_4$ and inner Cr_2O_3 scale.

The Ce/Co coating improved the performance of these steels. The chromium evaporation of the coated steels was lower than the uncoated steels. When the edges of the coated steels were uncoated, the chromium evaporation of different coated steels was dissimilar; it decreased by a factor of 10, compared to the uncoated ones. However, the coated steels with coated edges had at least 60 times less chromium evaporation than the uncoated ones and the chromium evaporation was similar for all steels. The experiments showed that the uncoated edges on the coated steels had higher chromium evaporation than would have been expected from the data obtained on uncoated specimens.

The Ce/Co coating reduced the oxidation of the steels compared to the uncoated ones. The steels showed differences in oxidation behaviour when uncoated but similar oxidation behaviour when coated. This might be because of the reactive elements in the coating. However, when the concentration of reactive elements in the coating was increased, no further improvement in the oxidation behaviour of the steels was observed. All the coated steels showed a similar oxide scale, with $(Co, Mn)_3O_4$ spinel on the top and Cr_2O_3 scale underneath. The low-cost steels, 441 and 444, showed SiO_2 enrichment at the metal-oxide interface. Nevertheless, the ASR of the Ce/Co coated steels was similar after 1,000 hours. Thus, coated low-cost steels such as AISI 441, 444, 430 seemed a better value proposition for their application as interconnects, due to their lower cost and greater availability than coated tailor-made steels such as Crofer 22 APU.

Future research should be focused on the investigation of the coating-steel combination at different temperatures. The beneficial effect of Ce is observed but is not fully understood. More fundamental research on the reactive element effect will be needed. Since the chromium evaporation of coated steels is very low, future research on steel development for interconnects should focus on the other degradation mechanisms.

Bibliography

[1] Arnab Choudhury, H. Chandra, and A. Arora. *Application of solid oxide fuel cell technology for power generation - A review.* Apr. 2013. DOI: 10.1016/j.rser.2012.11.031.

[2] *Manufacturing Cost Analysis of 100 and 250 kW Fuel Cell Systems for Primary Power and Combined Heat and Power Applications.* Tech. rep. Battelle Memorial Institute, 2016, pp. 1–289. URL: https://www.energy.gov/sites/prod/files/2016/07/f33/fcto_battelle_mfg_cost_analysis_pp_chp_fc_systems.pdf.

[3] *Manufacturing Cost Analysis of 1, 5, 10 and 25 kW Fuel Cell Systems for Primary Power and Combined Heat and Power Applications.* Tech. rep. Battelle Memorial Institute, 2017, p. 293. URL: https://www.energy.gov/sites/prod/files/2018/02/f49/fcto_battelle_mfg_cost_analysis_1_to_25kw_pp_chp_fc_systems_jan2017_0.pdf.

[4] Robert Steinberger-Wilckens. "Introduction to Fuel Cell Basics". In: *Advances in Medium and High Temperature Solid Oxide Fuel Cell Technology.* Ed. by Marta Boaro and Aricò Antonino Salvatore. Springer International Publishing, 2017, pp. 1–29. ISBN: 978-3-319-46145-8. DOI: https://doi.org/10.1007/978-3-319-46146-5.

[5] Timothy E. Lipman and Adam Z. Weber, eds. *Fuel cells and hydrogen production.* Springer-Verlag New York, 2019, pp. 1–1179. ISBN: 978-1-4939-7790-1.

[6] John Bøgild Hansen. "Solid Oxide Fuel Cells - Marketing Issues". In: *Fuel Cells.* Ed. by Klaus-Dieter Kreuer. New York, NY: Springer New York, 2013, pp. 1–7. ISBN: 978-1-4614-5784-8. DOI: 10.1007/978-1-4614-5785-5. URL: http://link.springer.com/10.1007/978-1-4614-5785-5.

[7] A. Boudghene Stambouli and E. Traversa. "Solid oxide fuel cells (SOFCs): a review of an environmentally clean and efficient source of energy". In: *Renewable and Sustainable Energy Reviews* 6.5 (Oct. 2002), pp. 433–455. ISSN: 1364-0321. DOI: 10.1016/S1364-0321(02)00014-X.

[8] Subhash C. Singhal. "Solid Oxide Fuel Cells: Past, Present and Future". In: *Green Energy and Technology.* Ed. by John T.S. Irvine and Paul Connor. Vol. 55. Springer Verlag, 2013, pp. 1–23. ISBN: 978-1-4471-4456-4. DOI: 10.1007/978-1-4471-4456-4{_}1.

[9] R Mark Ormerod. "Solid oxide fuel cells". In: *Chemical Society Reviews* 32.1 (2003), pp. 17–28. ISSN: 0306-0012. DOI: 10.1039/B105764M.

[10] Nguyen Q Minh. "Ceramic Fuel Cells". In: *Journal of the American Ceramic Society* 76.3 (Mar. 1993), pp. 563–588. ISSN: 0002-7820. DOI: https://doi.org/10.1111/j.1151-2916.1993.tb03645.x.

[11] A. Tsoga et al. "Gadolinia-doped ceria and yttria stabilized zirconia interfaces: regarding their application for SOFC technology". In: *Acta Materialia* 48.18-19 (Dec. 2000), pp. 4709–4714. ISSN: 1359-6454. DOI: 10.1016/S1359-6454(00)00261-5.

[12] Kevin Kendall and Michaela Kendall. *High-temperature Solid Oxide Fuel Cells for the 21st Century*. Elsevier, 2016. ISBN: 9780124104532.

[13] M. Cassidy et al. "Anodes". In: *High-Temperature Solid Oxide Fuel Cells for the 21st Century: Fundamentals, Design and Applications: Second Edition*. Academic Press, Jan. 2016, pp. 133–160. ISBN: 978-0-12-410453-2. DOI: 10.1016/B978-0-12-410453-2.00005-1.

[14] S Badwal et al. "Review of Progress in High Temperature Solid Oxide Fuel Cells". In: *ChemInform* 46 (2014).

[15] Y. Ji, J. A. Kilner, and M. F. Carolan. "Electrical properties and oxygen diffusion in yttria-stabilised zirconia (YSZ)–La0.8Sr0.2MnO3±δ (LSM) composites". In: *Solid State Ionics* 176.9-10 (Mar. 2005), pp. 937–943. ISSN: 0167-2738. DOI: 10.1016/J.SSI.2004.11.019.

[16] L. Niewolak, F. Tietz, and W. J. Quadakkers. "Interconnects". In: *High-Temperature Solid Oxide Fuel Cells for the 21st Century: Fundamentals, Design and Applications: Second Edition*. Academic Press, Jan. 2016, pp. 195–254. ISBN: 978-0-12-410453-2. DOI: 10.1016/B978-0-12-410453-2.00007-5.

[17] Jeffrey W. Fergus. "Lanthanum chromite-based materials for solid oxide fuel cell interconnects". In: *Solid State Ionics* 171.1-2 (June 2004), pp. 1–15. ISSN: 01672738. DOI: 10.1016/j.ssi.2004.04.010.

[18] José Luis Córdova and Hooshang Heshmat. *Development of a Ceramic Heat Exchanger for Application as Solid Oxide Fuel Cell Cathode Air Preheater*. June 2016. DOI: 10.1115/POWER2016-59333.

[19] H. J. T Ellingham. "Reproducibilty of oxides and sulphides in metallurgical processes". In: *Journal of the Society of Chemical Industry* 63.5 (May 1944), pp. 125–160. ISSN: 03684075. DOI: 10.1002/jctb.5000630501.

[20] P. Kofstad. *High Temperature Corrosion*. 1st ed. Elsevier Applied Science Publishers Ltd., 1988. ISBN: 1-85166-154-9.

[21] Neil Birks, Gerald H Meier, and Frederick S Pettit. *Introduction to the High Temperature Oxidation of Metals*. 2nd ed. Cambridge: Cambridge University Press, 2006. ISBN: 9780521480420. DOI: DOI:10.1017/CBO9781139163903.

[22] Carl Wagner. "Beitrag zur Theorie des Anlaufvorgangs". In: *Zeitschrift für Physikalische Chemie* 21B.1 (Feb. 1933), pp. 25–41. ISSN: 2196-7156. DOI: 10.1515/ZPCH-1933-2105.

[23] David J. Young. *High temperature oxidation and corrosion of metals*. 2nd ed. Elsevier Ltd., 2016, p. 733. ISBN: 978-0-08-100101-1. DOI: https://doi.org/10.1016/C2014-0-00259-6.

[24] Paul E Blackburn, Michael Hoch, and Herrick L Johnston. "The Vaporization of Molybdenum and Tungsten Oxides". In: *The Journal of Physical Chemistry* 62.7 (July 1958), pp. 769–773. ISSN: 0022-3654. DOI: 10.1021/j150565a001.

[25] M. Stanislowski et al. "Reduction of chromium vaporization from SOFC interconnectors by highly effective coatings". In: *Journal of Power Sources* 164.2 (Feb. 2007), pp. 578–589. ISSN: 03787753. DOI: 10.1016/j.jpowsour.2006.08.013.

[26] L. Mikkelsen, S. Linderoth, and J. B. Bilde-Sørensen. "The effect of silicon addition on the high temperature oxidation of a Fe-Cr alloy". In: *Materials Science Forum*.

Vol. 461-464. I. Trans Tech Publications Ltd, 2004, pp. 117–122. DOI: 10.4028/www.scientific.net/msf.461-464.117.

[27] D. Caplan and M. Cohen. "The Volatilization of Chromium Oxide". In: *Journal of The Electrochemical Society* 108.5 (1961), p. 438. DOI: 10.1149/1.2428106.

[28] Elizabeth J. Opila et al. "Theoretical and Experimental Investigation of the Thermochemistry of CrO 2 (OH) 2 (g)". In: *The Journal of Physical Chemistry A* 111.10 (Mar. 2007), pp. 1971–1980. ISSN: 1089-5639. DOI: 10.1021/jp0647380.

[29] Bartley B. Ebbinghaus. "Thermodynamics of gas phase chromium species: The chromium oxides, the chromium oxyhydroxides, and volatility calculations in waste incineration processes". In: *Combustion and Flame* 93.1-2 (Apr. 1993), pp. 119–137. ISSN: 0010-2180. DOI: 10.1016/0010-2180(93)90087-J.

[30] C S Tedmon. "The Effect of Oxide Volatilization on the Oxidation Kinetics of Cr and Fe-Cr Alloys". In: *Journal of The Electrochemical Society* 113.8 (1966), p. 766. ISSN: 0013-4651. DOI: 10.1149/1.2424115.

[31] Bagas Pujilaksono et al. "Paralinear oxidation of chromium in O 2 + H 2O environment at 600-700 °c". In: *Oxidation of Metals* 70.3-4 (Oct. 2008), pp. 163–188. ISSN: 0030770X. DOI: 10.1007/s11085-008-9114-1.

[32] Hai V Pham, Masaki Kurata, and Martin Steinbrueck. *Steam Oxidation of Silicon Carbide at High Temperatures for the Application as Accident Tolerant Fuel Cladding, an Overview*. 2021. DOI: 10.3390/thermo1020011.

[33] Roger C. Reed. *The Superalloys*. Cambridge: Cambridge University Press, 2006. ISBN: 9780511541285. DOI: 10.1017/CBO9780511541285.

[34] W. Z. Zhu and S. C. Deevi. "Opportunity of metallic interconnects for solid oxide fuel cells: A status on contact resistance". In: *Materials Research Bulletin* 38.6 (May 2003), pp. 957–972. ISSN: 00255408. DOI: 10.1016/S0025-5408(03)00076-X.

[35] Jeffrey Fergus et al. "Interconnects". In: *Solid Oxide Fuel Cells - Materials Properties and Performance*. CRC Press, Apr. 2016, pp. 195–228. ISBN: 9780429143649. DOI: 10.1201/9781420088847-8.

[36] Angeliki Brouzgou, Anatoly Demin, and Panagiotis Tsiakaras. "Interconnects for Solid Oxide Fuel Cells". In: *Advances in Medium and High Temperature Solid Oxide Fuel Cell Technology*. Ed. by Marta Boaro and Aricò Antonino Salvatore. Cham: Springer International Publishing, 2017, pp. 119–153. ISBN: 978-3-319-46146-5. DOI: 10.1007/978-3-319-46146-5.

[37] San Ping Jiang and Xinbing Chen. "Chromium deposition and poisoning of cathodes of solid oxide fuel cells - A review". In: *International Journal of Hydrogen Energy* 39.1 (Jan. 2014), pp. 505–531. ISSN: 03603199. DOI: 10.1016/j.ijhydene.2013.10.042.

[38] E. Konysheva et al. "Chromium vaporization of the ferritic steel Crofer22APU and ODS Cr5Fe1Y2O3 alloy". In: *Journal of Materials Science* 42.14 (July 2007), pp. 5778–5784. ISSN: 00222461. DOI: 10.1007/s10853-006-1194-1.

[39] G. V. Samsonov. "Electrical and Magnetic Properties". In: *The Oxide Handbook*. Boston, MA: Springer US, 1973, pp. 263–319. DOI: 10.1007/978-1-4615-9597-7{_}5.

[40] Keqin Huang, Peggy Y. Hou, and John B. Goodenough. "Reduced area specific resistance for iron-based metallic interconnects by surface oxide coatings". In:

Materials Research Bulletin 36.1-2 (Jan. 2001), pp. 81–95. ISSN: 00255408. DOI: 10.1016/S0025-5408(01)00506-2.

[41] Lauri Holappa. "Secondary Steelmaking". In: *Treatise on Process Metallurgy*. Vol. 3. Elsevier, Jan. 2014, pp. 301–345. ISBN: 978-0-08-096988-6. DOI: 10.1016/B978-0-08-096988-6.00012-2.

[42] Paul D. Jablonski, Christopher J. Cowen, and John S. Sears. "Exploration of alloy 441 chemistry for solid oxide fuel cell interconnect application". In: *Journal of Power Sources* 195.3 (Feb. 2010), pp. 813–820. ISSN: 03787753. DOI: 10.1016/j.jpowsour.2009.08.023.

[43] J. Froitzheim et al. "Development of high strength ferritic steel for interconnect application in SOFCs". In: *Journal of Power Sources* 178.1 (Mar. 2008), pp. 163–173. ISSN: 03787753. DOI: 10.1016/j.jpowsour.2007.12.028.

[44] W.J. Quadakkers et al. "Metallic interconnectors for solid oxide fuel cells – a review". In: 20.2 (), pp. 115–127. ISSN: 0960-3409.

[45] D. L. Douglass and J. S. Armijo. "The influence of manganese and silicon on the oxidation behavior of Co-20Cr". In: *Oxidation of Metals* 3.2 (Mar. 1971), pp. 185–202. ISSN: 0030770X. DOI: 10.1007/BF00603486.

[46] B. A. Pint. "Experimental observations in support of the dynamic-segregation theory to explain the reactive-element effect". In: *Oxidation of Metals* 45.1-2 (1996), pp. 1–37. ISSN: 0030770X. DOI: 10.1007/BF01046818.

[47] P Y Hou and J Stringer. "The effect of reactive element additions on the selective oxidation, growth and adhesion of chromia scales". In: *Materials Science and Engineering: A* 202.1 (1995), pp. 1–10. ISSN: 0921-5093. DOI: https://doi.org/10.1016/0921-5093(95)09798-8.

[48] R. Prescott and M. J. Graham. "The formation of aluminum oxide scales on high-temperature alloys". In: *Oxidation of Metals* 38.3-4 (Oct. 1992), pp. 233–254. ISSN: 0030770X. DOI: 10.1007/BF00666913.

[49] John Stringer. "The reactive element effect in high-temperature corrosion". In: *Materials Science and Engineering A* 120-121.PART 1 (Nov. 1989), pp. 129–137. ISSN: 09215093. DOI: 10.1016/0921-5093(89)90730-2.

[50] K. Przybylski, A. J. Garratt-Reed, and G. J. Yurek. "Grain Boundary Segregation of Yttrium in Chromia Scales". In: *Journal of The Electrochemical Society* 135.2 (Feb. 1988), pp. 509–517. ISSN: 0013-4651. DOI: 10.1149/1.2095646.

[51] D P Whittlef and J. Stringer. "Improvements in high temperature oxidation resistance by additions of reactive elements or oxide dispersions". In: *Philosophical Transactions of the Royal Society of London. Series A, Mathematical and Physical Sciences* 295.1413 (Feb. 1980), pp. 309–329. ISSN: 0080-4614. DOI: 10.1098/rsta.1980.0124.

[52] W. J. Quadakkers et al. "Differences in growth mechanisms of oxide scales formed on ODS and conventional wrought alloys". In: *Oxidation of Metals* 32.1-2 (Aug. 1989), pp. 67–88. ISSN: 0030770X. DOI: 10.1007/BF00665269.

[53] Jan Gustav Grolig, Jan Froitzheim, and Jan Erik Svensson. "Effect of Cerium on the Electrical Properties of a Cobalt Conversion Coating for Solid Oxide Fuel Cell Interconnects - A Study Using Impedance Spectroscopy". In: *Electrochimica Acta*

184 (Dec. 2015), pp. 301–307. ISSN: 00134686. DOI: 10.1016/j.electacta.2015.10.111.

[54] S. Fontana, S. Chevalier, and G. Caboche. "Metallic interconnects for solid oxide fuel cell: Performance of reactive element oxide coating during 10, 20 and 30 months exposure". In: *Oxidation of Metals* 78.5-6 (Dec. 2012), pp. 307–328. ISSN: 0030770X. DOI: 10.1007/s11085-012-9308-4.

[55] S. Fontana et al. "Metallic interconnects for SOFC: Characterisation of corrosion resistance and conductivity evaluation at operating temperature of differently coated alloys". In: *Journal of Power Sources* 171.2 (Sept. 2007), pp. 652–662. ISSN: 03787753. DOI: 10.1016/j.jpowsour.2007.06.255.

[56] J. G. Grolig, J. Froitzheim, and J. E. Svensson. "Coated stainless steel 441 as interconnect material for solid oxide fuel cells: Oxidation performance and chromium evaporation". In: *Journal of Power Sources* 248 (Feb. 2014), pp. 1007–1013. ISSN: 03787753. DOI: 10.1016/j.jpowsour.2013.08.089.

[57] D. Naumenko, B. A. Pint, and W. J. Quadakkers. *Current Thoughts on Reactive Element Effects in Alumina-Forming Systems: In Memory of John Stringer*. Aug. 2016. DOI: 10.1007/s11085-016-9625-0.

[58] Bruce A. Pint. *Progress in Understanding the Reactive Element Effect Since the Whittle and Stringer Literature Review*. Tech. rep.

[59] S. Chevalier. "What did we learn on the reactive element effect in chromia scale since Pfeil's patent?" In: *Materials and Corrosion* 65.2 (Feb. 2014), pp. 109–115. ISSN: 09475117. DOI: 10.1002/maco.201307310.

[60] *High-Temperature Fuel Cell Achieves Lifetime of More Than 11 Years*. Tech. rep. Forschungszentrum Jülich, Feb. 2019. URL: http://www.hpsc-terrsys.de/SharedDocs/Pressemitteilungen/UK/EN/2019/2019-02-07-sofc-en.html.

[61] Nima Shaigan et al. "A review of recent progress in coatings, surface modifications and alloy developments for solid oxide fuel cell ferritic stainless steel interconnects". In: *Journal of Power Sources* 195.6 (Mar. 2010), pp. 1529–1542. ISSN: 03787753. DOI: 10.1016/j.jpowsour.2009.09.069.

[62] Joelle C.W. Mah et al. "Metallic interconnects for solid oxide fuel cell: A review on protective coating and deposition techniques". In: *International Journal of Hydrogen Energy* 42.14 (Apr. 2017), pp. 9219–9229. ISSN: 03603199. DOI: 10.1016/j.ijhydene.2016.03.195.

[63] K H Tan, H A Rahman, and H Taib. "Coating layer and influence of transition metal for ferritic stainless steel interconnector solid oxide fuel cell: A review". In: *International Journal of Hydrogen Energy* 44.58 (2019), pp. 30591–30605. ISSN: 0360-3199. DOI: https://doi.org/10.1016/j.ijhydene.2019.06.155.

[64] Zhenguo Yang et al. "Conductive protection layers on oxidation resistant alloys for SOFC interconnect applications". In: *Surface and Coatings Technology* 201.7 (Dec. 2006), pp. 4476–4483. ISSN: 0257-8972. DOI: 10.1016/J.SURFCOAT.2006.08.082.

[65] W. J. Quadakkers et al. "Compatibility of perovskite contact layers between cathode and metallic interconnector plates of SOFCs". In: *Solid State Ionics* 91.1-2 (Oct. 1996), pp. 55–67. ISSN: 0167-2738. DOI: 10.1016/S0167-2738(96)00425-0.

[66] Anthony Petric and Hang Ling. "Electrical conductivity and thermal expansion of spinels at elevated temperatures". In: *Journal of the American Ceramic Society*

90.5 (May 2007), pp. 1515–1520. ISSN: 00027820. DOI: 10.1111/j.1551-2916.2007.01522.x.

[67] Yngve Larring and Truls Norby. "Spinel and Perovskite Functional Layers Between Plansee Metallic Interconnect (Cr-5 wt % Fe-1 wt % Y[sub 2]O[sub 3]) and Ceramic (La[sub 0.85]Sr[sub 0.15])[sub 0.91]MnO[sub 3] Cathode Materials for Solid Oxide Fuel Cells". In: *Journal of The Electrochemical Society* 147.9 (2000), p. 3251. ISSN: 00134651. DOI: 10.1149/1.1393891.

[68] Zhenguo Yang et al. "(Mn,Co)3O4 spinel coatings on ferritic stainless steels for SOFC interconnect applications". In: *International Journal of Hydrogen Energy* 32.16 (Nov. 2007), pp. 3648–3654. ISSN: 0360-3199. DOI: 10.1016/J.IJHYDENE.2006.08.048.

[69] J. Froitzheim et al. "Long term study of Cr evaporation and high temperature corrosion behaviour of Co coated ferritic steel for solid oxide fuel cell interconnects". In: *Journal of Power Sources* 220 (Dec. 2012), pp. 217–227. ISSN: 03787753. DOI: 10.1016/j.jpowsour.2012.06.092.

[70] Belma Talic et al. "Comparison of iron and copper doped manganese cobalt spinel oxides as protective coatings for solid oxide fuel cell interconnects". In: *Journal of Power Sources* 372 (Dec. 2017), pp. 145–156. ISSN: 03787753. DOI: 10.1016/j.jpowsour.2017.10.060.

[71] Carlos Bernuy-Lopez et al. "The Time for Industrialization Has Come: A Pre-Coated Solution for the GW Scale". In: *ECS Transactions* 103.1 (2021), pp. 1803–1808. ISSN: 1938-5862. DOI: 10.1149/10301.1803ecst.

[72] D. E. Alman and P. D. Jablonski. "Effect of minor elements and a Ce surface treatment on the oxidation behavior of an Fe-22Cr-0.5Mn (Crofer 22 APU) ferritic stainless steel". In: *International Journal of Hydrogen Energy* 32.16 (Nov. 2007), pp. 3743–3753. ISSN: 03603199. DOI: 10.1016/j.ijhydene.2006.08.032.

[73] S. Chevalier et al. "The reactive element effect on thermally grown chromia scale residual stress". In: *Materials Science and Engineering A* 343.1-2 (Feb. 2003), pp. 257–264. ISSN: 09215093. DOI: 10.1016/S0921-5093(02)00359-3.

[74] S. Canovic et al. "Oxidation of Co- and Ce-nanocoated FeCr steels: A microstructural investigation". In: *Surface and Coatings Technology* 215 (Jan. 2013), pp. 62–74. ISSN: 02578972. DOI: 10.1016/j.surfcoat.2012.08.096.

[75] T. Brylewski et al. "Influence of Gd deposition on the oxidation behavior and electrical properties of a layered system consisting of Crofer 22 APU and MnCo2O4 spinel". In: *International Journal of Hydrogen Energy* 46.9 (Feb. 2021), pp. 6775–6791. ISSN: 0360-3199. DOI: 10.1016/J.IJHYDENE.2020.11.169.

[76] Jan Froitzheim and Jan-Erik Svensson. *Multifunctional Nano-Coatings for SOFC Interconnects*. Apr. 2011. DOI: 10.1149/1.3570248.

[77] Wei Qu et al. "Yttrium, cobalt and yttrium/cobalt oxide coatings on ferritic stainless steels for SOFC interconnects". In: *Journal of Power Sources* 157.1 (June 2006), pp. 335–350. ISSN: 03787753. DOI: 10.1016/j.jpowsour.2005.07.052.

[78] Anders Harthøj, Tobias Holt, and Per Møller. "Oxidation behaviour and electrical properties of cobalt/cerium oxide composite coatings for solid oxide fuel cell interconnects". In: *Journal of Power Sources* 281 (May 2015), pp. 227–237. ISSN: 03787753. DOI: 10.1016/j.jpowsour.2015.01.128.

[79] Mareddy Reddy and Jan Froitzheim. *Report on chemical stability of the coated interconnects*. Tech. rep. 06. 2020, pp. 1–17. URL: https://ec.europa.eu/research/participants/documents/downloadPublic?documentIds=080166e5d67d5ca9&appId=PPGMS.

[80] Jan Gustav Grolig, Jan Froitzheim, and Jan Erik Svensson. "Coated stainless steel 441 as interconnect material for solid oxide fuel cells: Evolution of electrical properties". In: *Journal of Power Sources* 284 (June 2015), pp. 321–327. ISSN: 03787753. DOI: 10.1016/j.jpowsour.2015.03.029.

[81] Claudia Goebel et al. "Long-term (4 year) degradation behavior of coated stainless steel 441 used for solid oxide fuel cell interconnect applications". In: *Journal of Power Sources* 449 (Feb. 2020). ISSN: 03787753. DOI: 10.1016/j.jpowsour.2019.227480.

[82] Hannes Falk-Windisch et al. "Chromium vaporization from mechanically deformed pre-coated interconnects in Solid Oxide Fuel Cells". In: *Journal of Power Sources* 297 (Aug. 2015), pp. 217–223. ISSN: 03787753. DOI: 10.1016/j.jpowsour.2015.07.085.

[83] Arve Holt and Per Kofstad. "Electrical conductivity and defect structure of Cr2O3. I. High temperatures (>1000°C)". In: *Solid State Ionics* 69.2 (1994), pp. 127–136. ISSN: 0167-2738. DOI: https://doi.org/10.1016/0167-2738(94)90401-4.

[84] Arve Holt and Per Kofstad. "Electrical conductivity and defect structure of Cr2O3. II. Reduced temperatures (<1000°C)". In: *Solid State Ionics* 69.2 (1994), pp. 137–143. ISSN: 0167-2738. DOI: https://doi.org/10.1016/0167-2738(94)90402-2.

[85] L. Latu-Romain et al. "Duplex n- and p-Type Chromia Grown on Pure Chromium: A Photoelectrochemical and Microscopic Study". In: *Oxidation of Metals* 86.5 (Sept. 2016), pp. 497–509. ISSN: 1573-4889. DOI: 10.1007/s11085-016-9648-6.

[86] L. Latu-Romain et al. "The Role of Oxygen Partial Pressure on the Nature of the Oxide Scale on a NiCr Model Alloy". In: *Oxidation of Metals* 88.3 (Nov. 2017), pp. 481–493. ISSN: 1573-4889. DOI: 10.1007/s11085-016-9670-8.

[87] Arve Holt and Per Kofstad. "Electrical conductivity of Cr2O3 doped with TiO2". In: *Solid State Ionics* 117.1-2 (Feb. 1999), pp. 21–25.

[88] H. Nagai, T. Fujikawa, and K. Shoji. "Electrical Conductivity of Cr2O3 Doped with La2O3, Y2O3 and NiO". In: *Transactions of the Japan Institute of Metals* 24.8 (1983), pp. 581–588.

[89] Arve Holt and Per Kofstad. "Electrical conductivity and defect structure of Mg-doped Cr2O3". In: *Solid State Ionics* 100.3-4 (Oct. 1997), pp. 201–209. ISSN: 0167-2738. DOI: 10.1016/S0167-2738(97)00352-4.

[90] P. Huczkowski et al. "Growth mechanisms and electrical conductivity of oxide scales on ferritic steels proposed as interconnect materials for SOFC's". In: *Fuel Cells* 6.2 (Apr. 2006), pp. 93–99. ISSN: 16156846. DOI: 10.1002/fuce.200500110.

[91] Julian A. Crawford and Robert W. Vest. "Electrical Conductivity of Single-Crystal Cr2O3". In: *Journal of Applied Physics* 35.8 (Aug. 1964), pp. 2413–2418. ISSN: 0021-8979. DOI: 10.1063/1.1702871.

[92] J. H. Park and K. Natesan. "Electronic transport in thermally grown Cr2O3". In: *Oxidation of Metals 1990 33:1* 33.1 (Feb. 1990), pp. 31–54. ISSN: 1573-4889. DOI: 10.1007/BF00665668.

[93] B. Gillot et al. “Electrical conductivity of copper and nickel manganites in relation with the simultaneous presence of Mn3+ and Mn4+ ions on octahedral sites of the spinel structure”. In: *Solid State Ionics* 51.1-2 (Mar. 1992), pp. 7–9. ISSN: 0167-2738. DOI: 10.1016/0167-2738(92)90337-O.

[94] K. H. Tan, H. A. Rahman, and H. Taib. “Ba0.5Sr0.5Co0.8Fe0.2O3-δ-Sm0.2Ce0.8O1.9 carbonate perovskite coating on ferritic stainless steel interconnect for low temperature solid oxide fuel cells”. In: *Materials Chemistry and Physics* 254 (Nov. 2020), p. 123433. ISSN: 02540584. DOI: 10.1016/j.matchemphys.2020.123433.

[95] Manuel Bianco, Jan Pieter Ouweltjes, and Jan Van herle. “Degradation analysis of commercial interconnect materials for solid oxide fuel cells in stacks operated up to 18000 hours”. In: *International Journal of Hydrogen Energy* 44.59 (Nov. 2019), pp. 31406–31422. ISSN: 03603199. DOI: 10.1016/j.ijhydene.2019.09.218.

[96] A. Navrotsky and O. J. Kleppa. “The thermodynamics of cation distributions in simple spinels”. In: *Journal of Inorganic and Nuclear Chemistry* 29.11 (Nov. 1967), pp. 2701–2714. ISSN: 0022-1902. DOI: 10.1016/0022-1902(67)80008-3.

[97] Claudia Goebel et al. “Does the conductivity of interconnect coatings matter for solid oxide fuel cell applications?” In: *Journal of Power Sources* 383 (Apr. 2018), pp. 110–114. ISSN: 03787753. DOI: 10.1016/j.jpowsour.2018.02.060.

[98] J Andreas Schuler et al. “Cr-poisoning in (La,Sr)(Co,Fe)O3 cathodes after 10,000h SOFC stack testing”. In: *Journal of Power Sources* 211 (2012), pp. 177–183. ISSN: 0378-7753. DOI: https://doi.org/10.1016/j.jpowsour.2012.03.045.

[99] J. Froitzheim et al. “Investigation of Chromium Volatilization from FeCr Interconnects by a Denuder Technique”. In: *Journal of The Electrochemical Society* 157.9 (2010), B1295. ISSN: 00134651. DOI: 10.1149/1.3462987.

[100] J. Michael Hollas. *Modern Spectroscopy*. 4th ed. 2013, pp. 1–482. ISBN: 978-1-118-68160-2.

[101] Marie-Christine Fournier-Salaün and Philippe Salaün. “Quantitative determination of hexavalent chromium in aqueous solutions by UV-Vis spectrophotometer”. In: *Central European Journal of Chemistry 2007 5:4* 5.4 (Dec. 2007), pp. 1084–1093. ISSN: 1644-3624. DOI: 10.2478/S11532-007-0038-4.

[102] Weilie Zhou et al. “Fundamentals of Scanning Electron Microscopy (SEM)”. In: *Scanning Microscopy for Nanotechnology: Techniques and Applications*. Ed. by Weilie Zhou and Zhong Lin Wang. Springer, New York, NY, 2006, pp. 1–40. ISBN: 978-0-387-39620-0. DOI: 10.1007/978-0-387-39620-0{_}1.

[103] R. F. Egerton. *Physical principles of electron microscopy: An introduction to TEM, SEM, and AEM, second edition*. 2nd ed. Springer International Publishing, Jan. 2016, pp. 1–196. ISBN: 978-3-319-39877-8. DOI: 10.1007/978-3-319-39877-8.

[104] Yoshio Waseda, Eiichiro Matsubara, and Kozo Shinoda. *X-Ray Diffraction Crystallography*. Springer Berlin Heidelberg, 2011, pp. 67–106. ISBN: 978-3-642-44255-1. DOI: 10.1007/978-3-642-16635-8{_}3.

[105] Jan Gustav Grolig. “Coated Ferritic Stainless Steels as Interconnects in Solid Oxide Fuel Cells - Material Development and Electrical Properties”. PhD thesis. Chalmers University of Technology, Jan. 2015. ISBN: 978-91-7597-234-3. URL: https://research.chalmers.se/en/publication/220089.

[106] Jun Shu et al. “The effects of molybdenum addition on high temperature oxidation behavior at 1,000 °c of type 444 ferritic stainless steel”. In: *Oxidation of Metals* 78.3-4 (Oct. 2012), pp. 253–267. ISSN: 0030770X. DOI: 10.1007/s11085-012-9304-8.

[107] Hannes Falk-Windisch, Jan Erik Svensson, and Jan Froitzheim. “The effect of temperature on chromium vaporization and oxide scale growth on interconnect steels for Solid Oxide Fuel Cells”. In: *Journal of Power Sources* 287 (Aug. 2015), pp. 25–35. ISSN: 03787753. DOI: 10.1016/j.jpowsour.2015.04.040.

[108] Tien-Fu Chen et al. “Volume and Grain Boundary Diffusion of Chromium in Ni-Base Ni-Cr-Fe Alloys”. In: *MATERIALS TRANSACTIONS* 44.1 (2003), pp. 40–46. DOI: 10.2320/matertrans.44.40.

[109] G. Calvarin, R. Molins, and A. M. Huntz. “Oxidation Mechanism of Ni-20Cr Foils and Its Relation to the Oxide-Scale Microstructure”. In: *Oxidation of Metals* 53.1-2 (2000), pp. 25–48. ISSN: 0030770X. DOI: 10.1023/A:1004578513020.

[110] S J Rothman, L J Nowicki, and G E Murch. “Self-diffusion in austenitic Fe-Cr-Ni alloys”. In: *Journal of Physics F: Metal Physics* 10.3 (1980), pp. 383–398. ISSN: 0305-4608. DOI: 10.1088/0305-4608/10/3/009.

[111] T M Devine. “Kinetics of sensitization and de-sensitization of duplex 308 stainless steel”. In: *Acta Metallurgica* 36.6 (1988), pp. 1491–1501. ISSN: 0001-6160. DOI: https://doi.org/10.1016/0001-6160(88)90216-7.

[112] Xu Wang and Jerzy A Szpunar. “Effects of grain sizes on the oxidation behavior of Ni-based alloy 230 and N”. In: *Journal of Alloys and Compounds* 752 (2018), pp. 40–52. ISSN: 0925-8388. DOI: https://doi.org/10.1016/j.jallcom.2018.04.173.

[113] T. Sand et al. “Effective Reduction of Chromium-oxy-hydroxide Evaporation from Ni-Base Alloy 690”. In: *Oxidation of Metals* 92.3-4 (Oct. 2019), pp. 259–279. ISSN: 15734889. DOI: 10.1007/s11085-019-09935-9.

[114] Hannes Falk-Windisch et al. “Co- and Ce/Co-coated ferritic stainless steel as interconnect material for Intermediate Temperature Solid Oxide Fuel Cells”. In: *Journal of Power Sources* 343 (2017), pp. 1–10. ISSN: 03787753. DOI: 10.1016/j.jpowsour.2017.01.045.

[115] Matthieu Tomas et al. “Cu-Based Coatings for IT-SOFC Applications”. In: *ECS Transactions* 91.1 (July 2019), pp. 2291–2298. ISSN: 1938-6737. DOI: 10.1149/09101.2291ecst.

[116] W. David Kingery, H. K. Bowen, and Donald R. Uhlmann. *Introduction to Ceramics, 2nd Edition*. 1976, p. 1056. ISBN: 978-0-471-47860-7.

Abbreviations

ASR Area Specific Resistance

BOP Balance of Plant

BSE Back-scattered Electron

CGO Gadolinia Doped Ceria

CHP combined Heat and Power

EDX Energy Dispersive X-ray Spectroscopy

FSS Ferritic Stainless Steel

MCO Manganese Cobalt oxide

PEMFC Proton-exchange membrane fuel cell

PVD Physical Vapor Deposition

RE Reactive Element

SE Secondary Electron

SEM Scanning Electron Microscopy

SOEC Solid Oxide Electrolysis Cell

SOFC Solid Oxide Fuel Cell

TEC Thermal Expansion Coefficient

XRD X-ray Diffraction

List of Figures

List of Tables